Impact of Trivalent Dopants in the Electrochemical Performance of Zinc cobaltite

By

V. YAZHINI

(21PPH025)

A Thesis submitted to the

AVINASHILINGAM INSTITUTE FOR HOME SCIENCE AND HIGHER EDUCATION FOR WOMEN, COIMBATORE – 641 043.

In partial fulfilment of the requirements for the Degree of

MASTER OF SCIENCE IN PHYSICS

MAY 2023

Impact of Trivalent Dopants in the Electrochemical Performance of Zinc cobaltite

By

V.YAZHINI

(Reg No. 21PPH025)

Supervisor

Dr. B. Nalini

Department of Physics

A Thesis submitted to

AVINASHILINGAM INSTITUTE FOR HOME SCIENCE AND HIGHER EDUCATION FOR WOMEN, COIMBATORE – 641043

In partial Fulfillment of the Requirements of the Degree of

MASTER OF SCIENCE IN PHYSICS

MAY 2023

CERTIFIED AS A BONAFIDE RESEARCH WORK

12/05/23

Signature of Head of the Department

Dr. J. SHANTHI, M.Sc., M.Phil., Ph.D.,
Professor and Head
Department of Physics
Avinashilingam Institute for Home Science
and Higher Education For Women
Coimbatore - 641 043.

12/05/2023

Signature of the Supervisor

ACKNOWLEDGEMENT

I owe my sincere thanks to the Lord Almighty, the reverent founder **Dr. T. S. Avinashilingam Ayya** and **Amma Dr. Rajammal P. Devadas,** and my lovable parents. Without whom I should have been nothing, for showering their generous blessings upon us in all endeavors.

I wish to express my deep sense of reverential gratitude to the Chancellor **Prof. S. P Thyagarajan** Ph.D., M.D., D.S, FAMS, FNASc, FIMSA, FABMS, FFTM (Glasgow, UK), the Vice Chancellor. **Dr. V. Bharathi Harishankar** Ph.D., FRSA, and the Registrar **Dr.S. Kowsalya**, Ph.D. Avinashilingam Institute for Home Science and Higher Education for Women, Coimbatore for providing all the necessary facilities for the internship.

I wholeheartedly thank **Dr. G. Padmavathi**, Ph.D. Dean, School of Physical Science and Computational Science, Avinashilingam Institute for Home Science and Higher Education for Women, Coimbatore for her encouragement and generous help which was of great value.

I express my sincere gratitude to **Dr. (Mrs.) J. Shanthi**, M.Sc., M.Phil., Ph.D., Professor and Head – Department of Physics, Avinashilingam Institute for Home Science and Higher Education for Women, Coimbatore for her constant support and encouragement for all activities.

I express my heartiest thanks to my guide **Dr.(Mrs.) B. Nalini,** M.Sc., Ph.D., M.S (Edu.Mgt.), STA fellow, AIST Fellow (Japan), Assistant Professor, Avinashilingam Institute for Home Science and Higher Education for Women, University, Coimbatore, for her valuable guidance learned counsel, cordial treatment, keen interest, constant encouragement and care rendered throughout the course of my investigation.

I sincerely thank all **the staff members** of the Department of Physics, Avinashilingam Institute for Home Science and higher education for Women, Coimbatore, for their help and support.

I would like to express my special thanks to **my parents, friends** and all **well-wishers** for their constant encouragement, support and help in carrying out this work successfully.

V. YAZHINI

CONTENT

LIST OF FIGURES

LIST OF TABLES

CHAPTER I

INTRODUCTION

1.1 Introduction:

Batteries store electrical energy in the form of electrochemical reaction. It is also applicable to supercapacitors and fuel cells. They convert chemical energy produced from its constituents to electrical energy by performing oxidation, reduction and redox reaction. The mechanism that produces electrical energy from chemical energy is known as an electric battery. It makes use of controlled chemical processes, where the desired chemical process takes place electrochemically. An electrolyte, cathode, and an anode are some of the essential components of the battery. Anode and cathode are terms used to describe positive and negative electrodes, respectively. A separator acts as a barrier between the two electrodes to prevent short-circuiting. A battery is created by connecting these several electrochemical cells in series. Alessandro Volta created the first electric battery in the year 1800, which is popularly known as the voltaic pile. Batteries are divided into two categories based on their capacity to be recharged. [1]

- Primary Battery
- Secondary Battery

The standard cell potential E_0 is connected to every oxidation and reduction reaction. The thermodynamic equation can be used to calculate the standard cell potential as shown below.

$$\mathbf{E_0 = -\Delta G_0/ZF}$$

where,

ΔG_0 - standard Gibbs free energy

Z - Number of electrons exchanged

F - Faraday Constant

The overall theoretical cell voltage ΔE_0 is obtained by subtracting the negative electrode potential E_0 (-), from the positive electrode potential E_0 (+).

$$\mathbf{\Delta E_0 = E_0\,(+) - E_0\,(-)}$$

1.2 Primary Battery:

Primary batteries cannot be recharged. Chemical reactions occur in this type of cell irreversibly. Because there is no free or liquid electrolyte in these cells, they are often referred to as "dry cells". Primary batteries are affordable, lightweight, long-lasting, and simple to use. Devices like LEDs, kids' toys, memory backup, watches, etc. frequently use it.

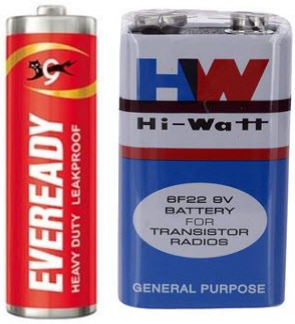

Fig 1.1 Primary Battery

1.2.1 Zinc Carbon Battery:

The zinc carbon battery, commonly known as the Leclanche cell, is a primary/non-rechargeable battery. The manganese dioxide cathode, zinc anode, and zinc chloride or ammonium chloride, employed as the electrolyte, are the components of the zinc carbon battery. These are frequently found in toys and flashlights. [2]

$$Zn + 2MnO_2 + 2NH_4Cl \rightarrow 2MnOOH + Zn\,(NH_3)2Cl_2$$

1.2.2 Alkaline Manganese Battery:

Alkaline manganese batteries are non-rechargeable and are often found in radios, toys, watches, and other electronic devices. These batteries use manganese dioxide as the cathode, zinc powder as the anode, and potassium hydroxide as the electrolyte. [3]

$$Zn + 2MnO_2 \rightarrow ZnO + Mn_2O_3 \qquad E=1.5\ V$$

Table 1.1 Types of Batteries and their applications

Battery Type	Characteristics	Applications
Zinc – Carbon	Common, low cost, variety of sizes	Radios, toys, instruments
Magnesium (Mg/MnO_2)	High capacity, long shelf life	Military and aircraft Radios
Mercury (Zn/HgO)	Very high capacity, long shelf life	Medical (hearing aids, pacemakers), photography
Alkaline ($Zn/Alkaline/MnO_2$)	Very popular, moderate cost, high performance	Most popular primary batteries
Silver/Zinc (Zn/Ag_2O)	Highest capacity, costly, flat discharge	Hearing aids, photography, pagers
Lithium/Soluble Cathode	High energy density, good performance, wide temp range	Wide range of applications with capacity between 1 – 10,000 Ah
Lithium/Solid Cathode	High energy density, low temp performance, long shelf life	Replacement for button and cylindrical cells
Lithium/Solid Electrolyte	Low power, extremely long shelf life	Memory circuits, medical electronics

1.3 Secondary Battery:

Secondary batteries can be recharged. By passing the current in the opposite direction as the discharge current, the cells can be quickly recharged. This kind of cell

undergoes a reversible chemical process. This set of batteries attracted widespread attention as a result of its uses for portable devices like smartphones, laptops, digital cameras, and other vehicles as well. Electronic equipment previously used Ni-Cd and Ni-Metal hybrid batteries. Later, Li-ion, Na-ion, and other types of batteries take their place. [4]

In reality, the Lead-Acid and Nickel-Cadmium batteries, which were created in the late 1850s and the early 1900s, respectively, are two of the oldest types of batteries. There were only two varieties of secondary batteries up until recently.

Lead-Acid Batteries are the original and most widely used rechargeable batteries. They are based on the electrochemical couple between lead and lead dioxide (Pb - PbO_2). Sulfuric acid, a substance that is widely utilized, serves as the electrolyte in these kinds of batteries.

Nickel-Cadmium Batteries are the name given to the second class of rechargeable batteries. They have a negative electrode made of Cadmium metal and a positive electrode made of Nickel Oxyhydroxide (Nickel Oxide). When it comes to the electrolyte, potassium hydroxide is used in an alkaline solution.

Two new types of rechargeable batteries have emerged in recent decades. They are the lithium-ion battery and the nickel-metal hydride battery. With its high specific energy and energy density values (150 Wh/kg and 400 Wh/L), the lithium-ion battery emerged as the market leader and a game-changer.

1.4 Components of a Battery:

The cathode (positive electrode), anode (negative electrode), and electrolyte are the three basic parts of a battery**.**

1.4.1 Anode:

The anode, which is a negative electrode, causes an oxidation reaction that discharges electrons into the external circuit. High reduction efficiency, high coulombic output, and superior electrical conductivity are required for anode materials. Different metals and metal oxides such as Li, SnO_2, Si, Ge, MoO_3, $NiMoO_4$, $CoFe_2O_4$, etc., are used as anode materials in lithium-ion batteries. Among various types of titanium oxides,

$Li_4Ti_5O_{12}$ (LTO) stands out as an excellent lithium storage material due to its “zero” strain during lithium ion insertion and fast lithium ion transport.

1.4.2 Cathode:

The cathode, which is a positive electrode, takes electrons from the external circuit through a reduction reaction. $LiCoO_2$ has been the cathode material of choice for industrial lithium-ion batteries for decades. The cathode materials ought to be highly structurally stable and effective oxidizers. Common cathode materials in lithium-ion batteries include $LiCoO_2$, $LiMn_2O_4$, $LiNiO_2$, $LiFePO_4$, and others. In this study, Zinc cobaltite is used as the cathode. [5]

1.4.3 Electrolyte:

The material through which lithium ions move from one electrode to another electrode is called an electrolyte. The electrolyte must be safe to handle, non-reactive to the electrodes, and have a high ionic conductivity with negligible electronic conduction. In lithium-ion batteries, $ZnCl_2$, KOH, and $LiPF_6$ are often used as electrolytes that are dissolved in EC: DMC in a volume ratio of 1:1. Aqueous electrolytes are utilized in the majority of modern batteries; however, lithium material will react with them. In this study, LiOH is used as the electrolyte. LiOH electrolyte enhances the electrochemical performance.

1.5 Electrochemical energy storage device:

Nowadays researchers are increasingly paying much attention to sustainable methods for storing energy. Many researchers are now concentrating their efforts on the development and exploration of novel materials for energy storage devices due to the limited supply of existing energy sources such as oil, coal, and natural gas, and escalating regional tensions. Because of these issues, sustainable renewable energy sources have been touted as an alternative to nonrenewable fuels. Deployment of renewable energy sources requires efficient and reliable energy storage devices due to their intermittent nature. High-performance electrochemical energy storage technologies with high power and energy densities are heralded to be the next-generation storage devices. Transition metal chalcogenides (TMCs) have sparked interest among electrode materials because of their intriguing electrochemical properties. Electrochemical energy storage covers all types of secondary batteries. Batteries convert chemical energy contained in its active materials into

electric energy by an electrochemical oxidation – reduction reaction. At present batteries are produced in many sizes for wide spectrum of applications. Commonly commercial accessible secondary batteries according to the used electrochemical system can be divided into the following basic groups:

- Standard batteries (Lead acid, Ni-Cd)
- Modern batteries (Ni-MH, Li–ion, Li-pol)
- Special batteries (Ag-Zn, Ni-H_2)
- Flow batteries (Br_2-Zn, vanadium redox)
- High-temperature batteries (Na-S, Na–metal chloride). [6]

1.5.1 Lead Acid Batteries:

The most common and widely used rechargeable batteries are lead-acid batteries. They have been a popular one for over a century. The capacity of lead-acid batteries ranges from small sealed cells with a capacity of 1 Ah to big cells with a capacity of 12,000 Ah. Lead-acid batteries are widely employed in the automotive sector, where they are generally used as SLI Batteries (Starting, Lighting, and Ignition) units. Lead-acid batteries are also used for energy storage, backup power, electric vehicles (including hybrid vehicles), communication systems, emergency lighting systems. Lead-acid batteries have a broad variety of uses due to their wide voltage ranges, various shapes and sizes, inexpensive cost, and relatively simple maintenance. Lead-acid batteries are the least priced alternative for any application and offer extremely good performance when compared to other secondary battery technologies. Lead-acid batteries have an electrical efficiency of 75 to 80%. They are excellent for energy storage (Uninterrupted Power Supplies, or UPS), as well as electric cars, because to their efficiency value. [7]

Fig 1.2 Lead Acid Battery

1.5.2 Nickel Cadmium Battery:

They are extremely durable, dependable, and have a very long lifespan. Nickel-cadmium batteries are rechargeable, with Nickel hydroxide on the positive electrode and

cadmium on the negative electrode. The battery's biggest drawback is its poor power efficiency. The reactions are switched around when charging and discharging. Digital cameras, calculators, computers, lamps, electric vehicles, space applications, etc. all use nickel-cadmium batteries in some capacity where higher power density is required. [8]

1.5.3 Nickel – Metal Hydride Battery:

A nickel-metal hydride battery is a secondary/rechargeable battery. Nickel hydroxide serves as the positive electrode while hydrogen serves as the negative electrode. At the positive electrode, an electrochemical reaction similar to that of a nickel-cadmium battery takes place, while at the negative electrode, hydrogen is absorbed. The energy density of a nickel metal hydride battery is approximately identical to that of a lithium-ion battery, and it has a capacity that is two to three times more than that of a nickel cadmium battery. It can be used in a variety of devices, including electric vehicles, power tools, computers, and emergency lighting. [9]

1.6 Lithium ion Battery:

With the development of society and the economy, exploring new and clean energy is becoming increasingly urgent. Lithium ion battery (LIB) has been one of the most important energy storage devices in various portable electronics because of its long cycling time, large energy density and no memory effect. Lithium batteries are electrochemical devices that are widely used as power sources. A lithium-ion (Li-ion) battery is an advanced battery technology that uses lithium ions as a key component of its electrochemistry. Li-ion batteries can use a number of different materials as electrodes. The most common combination is that of lithium cobalt oxide (cathode) and graphite (anode), which is most commonly found in portable electronic devices such as cellphones and laptops. Other cathode materials include lithium manganese oxide (used in hybrid electric and electric automobiles) and lithium iron phosphate. Li-ion batteries typically use ether (a class of organic compounds) as an electrolyte. A Li-ion battery is a type of rechargeable battery that uses the reversible reduction of lithium ions to store energy. The anode (negative electrode) of a conventional lithium-ion cell is typically graphite made from carbon. The cathode (positive electrode) is typically a metal oxide. The electrolyte is typically a lithium salt in an organic solvent. Lithium is the lightest metal and it can float on water. The electrochemical properties of lithium are excellent and it is also a highly reactive material. These properties give lithium the potential to achieve very high energy

and high-power density battery applications such as automotive and standby power. The theoretical specific storage capacity of Li is 3860 Ah/kg. In lithium batteries, lithium metal (or) lithium compound acts as an anode. A lithium cell can produce voltage from 1.5 V to 3 V based on the type of materials used. [10]

1.6.1 Types of Lithium-ion batteries:

Although lithium-ion technology is still developing, it has not yet reached its full maturity. In today's cells, the cathode is a combination of lithium and other premium metals, and the anode is composed of a mixture of graphite. It should be noted that every component of a battery theoretically has an energy density. With lithium-ion, the anode is well optimized and there aren't many design adjustments that can be made to improve performance. However, the cathode exhibits potential for improvement. The cathode material is the subject of current battery research. The electrolyte is a component that also has potential. In order for the anode and the cathode to react, an electrolyte is used as a reaction medium. [11]

Table 1.2 Classification of Lithium ion batteries

Chemical name	Material	Characteristics
Lithium Cobalt Oxide Also Lithium Cobaltate or lithium-ion-cobalt)	$LiCoO_2$ (60% Co)	High capacity; for cell phone laptop, camera.
Lithium Manganese Oxide Also Lithium Manganate or lithium-ion-manganese	$LiMn_2O_4$	Most safe; lower capacity than Li-cobalt but high specific power and long life.
Lithium Iron Phosphate	$LiFePO_4$	Power tools, e-bikes, EV, medical, hobbyist.
Lithium Nickel Manganese Cobalt Oxide, also lithium-manganese-cobalt-oxide	$LiNiMnCoO_2$ (10–20% Co)	

Lithium Nickel Cobalt Aluminium Oxide	$LiNiCoAlO_2$ 9% Co)	Gaining importance in electric powertrain and grid storage
Lithium Titanate	$Li_4Ti_5O_{12}$	

1.7 History of Lithium ion battery:

Research on rechargeable Li-ion batteries dates to the 1960s; one of the earliest examples is a CuF_2/Li battery developed by NASA in 1965. The breakthrough that produced the earliest form of the modern Li-ion battery was made by British chemist M. Stanley Whittingham in 1974, first used titanium disulfide (TiS_2) as a cathode material, which has a layered structure that can take in lithium ions without significant changes to its crystal structure. Significant improvements in energy density were achieved in the 1990s by replacing the soft carbon anode first with hard carbon. In 2010, the global lithium-ion battery production capacity was 20 gigawatt-hours. By 2016, it was 28 GWh, with 16.4 GWh in China. Global production capacity was 767 GWh in 2020, with China accounting for 75%. Whittingham, and Yoshino were awarded the 2019 Nobel Prize in Chemistry "for the development of lithium-ion batteries In April 2023 CATL announced that it would begin scaled-up production of a battery that produces 500 Wh/kg, the magic number for civil aircraft use. [12]

1.8 Principle of Lithium ion battery:

The primary goal of battery research is to build a cell having high specific energy, which will have a quick charging and can be cycled rapidly without losing its capacity. The reactants in the electrochemical reactions in a lithium-ion cell are materials of anode and cathode, both of which are compounds containing lithium atoms. Metals like zinc and lithium are often used as substrates for anodes. The electrolytes are selected in such a way that there should be an effective transport of Li-ion to the cathode during discharge. Lithium ion batteries are secondary batteries. In a battery there are two electrodes immersed in an electrolyte. When an external load is connected to these two electrodes, oxidation reaction starts occurring in one electrode and at the same time reduction occurs in other electrodes. The electrode, where oxidation takes place, the number of electrons

becomes excess. This electrode is referred as negative electrode or anode. During the process of charging, the current flows towards the positive plate and positive charge gets added to that plate and away from the negative plate. While discharging, the current flows away from the positive end towards the negative end in the opposite direction. [13]

1.9 Zinc Cobaltite:

Zinc cobaltite ($ZnCo_2O_4$) is a p-type semiconductor material with a spinel-type structure. This material has attracted the attention of several research groups due to its potential applications as an electrode for Li-ion batteries, as a catalyst, and in supercapacitors. In the gas sensors field, sensor devices based on $ZnCo_2O_4$ nanoparticles have displayed an excellent sensitivity to liquefied petroleum gas, H_2S, ethanol, acetone, and formaldehyde, probably due to their high surface area. When prior reports on the cobaltite-based electrodes are taken into account, $ZnCo_2O_4$ electrodes are more effective. Compared to simple metal oxides, they had more electrochemical activity and more complex redox processes, which led to superior capacitive performance. Recent studies have also shown that supercapacitors and Li-ion batteries can both benefit from high-performance electrochemical capabilities achieved by 1D $ZnCo_2O_4$ nanowires grown on conductive current collectors. It is anticipated that the composites of 1D $ZnCo_2O_4$ nanostructures, which are promising electroactive materials, will perform more capacitively than their binary oxide counterparts.

1.10 Advantages of Lithium-ion battery:

- High specific energy and high load capabilities with power cells.
- Long cycle and extend shelf-life; maintenance-free.
- High capacity, low internal resistance, good coulombic efficiency.
- Simple charge algorithm and reasonably short charge times. [14]
- Low self-discharge (less than half that of NiCd and NiMH).

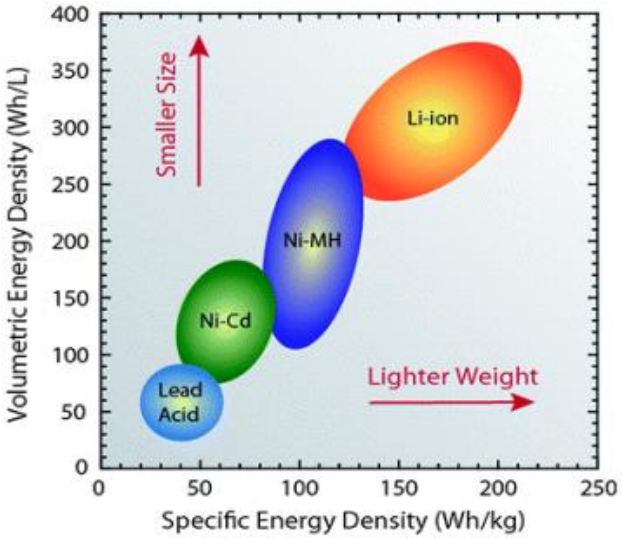

Fig 1.3 Volumetric energy density Vs. Gravimetric energy density of different rechargeable (secondary) batteries

1.11 Applications of Lithium-ion battery:

Industrial applications have particular power requirements; thus, battery selection is crucial. While the industry prioritizes durability and reliability, consumer items seek great energy density to achieve thin and beautiful designs. Industrial batteries often take up more space than those found in consumer goods, but they have a longer lifespan. [15]

- **In professional camera:**

  A significant number of professional cameras are still powered by nickel-cadmium batteries. This battery performed well at low temperatures and offered dependable service. Although nickel-cadmium batteries have one of the longest lifespans, they have a low energy density and require regular full discharges. The transition to nickel-metal-hydride is being driven by the demand for longer runtimes. Comparing this battery to nickel-cadmium, it gives up to 50% more energy. However, the large current spikes generated by digital cameras have a detrimental effect and shorten the nickel-metal-hydride battery's lifespan. The use of lithium-ion is on the rise. This chemical is the lightest and has the maximum energy density of all rechargeable. Negatives include a high price and a limitation on high currents.

- **For medical devices:**

The heart defibrillator is one of the most power-hungry portable medical gadgets. During the preparation process, the battery uses more than 10 ampere. It can take several shocks to restart the patient's heart. The battery must not impede providing the best patient care feasible. The medical sector is switching to lithium-ion. The reliable and affordable 18650 cells enable this. It's still difficult to create the quick, high-current bursts required for defibrillators. This problem can be solved by paralleling the cells and including current-limiting circuits that permit brief bursts of high current.

- **For power tools:**

Power tools operate in a hostile environment and need up to 50 amps of electricity. The tool must function in extreme heat and below zero degrees. The batteries must be resilient to vibration and shock. Nickel-cadmium batteries are used with the majority of power tools. With little success, nickel-metal-hydride has been tried. Although longevity is a challenge, innovative designs have made progress. Because it is too fragile, lithium-ion batteries cannot deliver high amperage. Lead-acid batteries are too heavy and don't produce power consistently. The tough and reliable nickel-cadmium has simply no adequate substitutes in the power tool industry.

1.12 Need for Zinc cobaltite:

Research works on Zinc cobaltite are still under study for the usage of lithium batteries. Zinc cobaltite as a spinel-structured metal oxide has more electrochemical activity and more complex redox processes, it finds many applications in lithium batteries and supercapacitors. The rare earth elements like Lanthanum and Dysprosium have not yet been doped with Zinc cobaltite. There aren't many reports on dopants that successfully increase electrochemical activity.

1.13 Objective:

- To evaluate the impact of Trivalent Dopants in Zinc cobaltite.
- To evaluate the electrochemical performance of Zinc cobaltite with dopants.

1.14 Methodology:

- To prepare Zinc cobaltite by Sol-gel method.
- To prepare Chromium, Lanthanum, and Dysprosium trivalent doped Zinc cobaltite samples.
- To characterize their structural and electrochemical studies.

CHAPTER II

REVIEW OF LITERATURE

Numerous metal oxides with spinel structures have been discovered for energy storage technology. Cobaltite (MCo_2O_4; M=Zn, Ni, Cu, Mn, etc.) has been regarded as an effective electrode material for lithium batteries and supercapacitor applications among the many known spinel-structured metal oxides due to its high electrochemical stability, an abundance of resources, and low cost. Many efforts have been made to improve the electrochemical performance of cobaltite, including developing composite materials, doping with suitable elements, and using various nanostructured morphologies. Zinc cobaltite acts as a cathode in many supercapacitors which gives higher efficiency. Zinc cobaltite-based supercapacitors and lithium batteries are discussed in this chapter.

2.1 Zinc cobaltite-based Supercapacitors:

[16] **Elham Samiei et.al., (2021)** intended for usage in energy applications with binary transitional metal oxides. In this research, a one-step hydrothermal approach was used to create a cheap 3D hierarchical $ZnCo_2O_4$ with flower-like morphology on nickel foam. The electrochemical observations indicate that this electrode has a high potential for usage in asymmetric supercapacitors. The specific capacitance of roughly 572 F/g at a scan rate of 10 mV/s and very high stability (94% after 5000 cycles) make this electrode appealing for use. Furthermore, at a current density of 0.5 A/g, the discharge time of this electrode was approximately 380 s, which is a pretty acceptable time. An electrode with unique designs suggests the use of elevated asymmetric supercapacitors.

[17] **Soundarya et.al., (2021)** determined that transitional metal oxides are widely used in energy storage systems due to their exceptional electrochemical activity and charge storage capacity. This research develops a unique (Ni,Cr:$ZnCo_2O_4$) electrode material for supercapacitor (SC) applications by doping Zinc cobaltite ($ZnCo_2O_4$) with Ni and Cr. Dopants aided electrochemical activity by acting as a conductivity booster, particle size reducer, and active site provider. In comparison, the doped sample produced an elevated capacitance value of 575 Fg^{-1} in the potential range of 0-0.6V using 1 M KOH solution as an electrolyte, which is greater than that of the pristine material, as well as enhanced cyclic stability from 82.2% to 90.24% for 2000 cycles. The developed asymmetric supercapacitor

device with Ni,Cr:$ZnCo_2O_4$ exhibits specific capacitance values of 30 Fg^{-1} and 73 Fg^{-1} at 0.75 Fg^{-1} employing Cu foil and Ni foam as current collectors. The device developed with doped sample and a Ni foam current collector has an energy density of 16.3 $WhKg^{-1}$ and a power density of 0.9 $KWKg^{-1}$, outperforming devices built with pure $ZnCo_2O_4$. The result of the Ni and Cr doped crystalline structured Zinc cobaltite device reveals substantial progress towards higher efficiency supercapacitor applications.

[18] **Juliet Christina Mary et.al., (2020)** researched to find out the hybrid nanocomposite material and biomass-derived N-doped activated carbon with variable shape, composition, and topologies which are used to create extremely effective supercapacitor devices. Several surfactants are used to create $NiCo_2O_4$ materials with various morphologies such as spherical, urchin, rod, and granular. The highest specific capacity of these electrode materials at 1 A g^{-1} in 2 M KOH is 419, 543, 506, and 456 C g^{-1}. Using various concentrations of $ZnCo_2O_4$ nanosheets, the optimum urchin-like $NiCo_2O_4$ is hybridized. The specific capacity for $NiCo_2O_4$@$ZnCo_2O_4$ was greatly improved by the hybridization method, reaching 1029 C g^{-1} at 1 A g^{-1}. (NZC2). Honeycomb porous patterned N-doped activated carbon is created using the *Ricinus communis* seed to create the hybridized supercapacitor device. With a high nitrogen concentration and a maximum specific capacity of 236 C g^{-1} at a current density of 1 Ag^{-1}, the synthesized material displays an interlinked pore structure. With a comparable power density of 1.62 kW kg^{-1} and the greatest energy density of 101.6 W h kg^{-1}, the hybrid supercapacitor device built of NZC_2 and N-doped activated carbon is the best.

[19] **Gutturu Rajasekhara Reddy et.al., (2020)** presents the hydrothermal synthesis of 3D-hierarchical peony-like $ZnCo_2O_4$ structures with 2D nanoflakes utilizing polyvinylpyrrolidone. The reaction time was changed to obtain two samples (ZCO-6h and ZCO-12h), while the other synthesis conditions remained constant. The ZCO-12h sample has a greater surface area (55.40 m^2g^{-1}) and pore size (24.69 nm) than the ZCO-6h sample, allowing for faster ion and electron transport. Electrochemical investigation revealed that the ZCO-12h electrode had a significant specific capacitance of 421.05 Fg^{-1}(31.52 Cg^{-1}) at 1 Ag^{-1} and outstanding cycle performance. Furthermore, the morphologic properties of the developed hierarchical materials greatly improved specific capacitance. The outstanding capacitive results suggest that 3D-$ZnCo_2O_4$ hierarchical peony-like structures made of 2D nanoflakes are suitable materials for high-performance supercapacitors.

[20] **Priya et.al., (2019)** executed a hydrothermal process and sodium hydroxide (NaOH) as a reducing agent, $ZnCo_2O_4$ nanoparticles have been effectively created. XRD investigation revealed the production of tiny cubic structures and quite well crystalline nanoparticles with diameters of 27 nm as assessed by the Debye Scherrer technique. DLS from zeta potential analysis was used to determine the particle size distribution and potential stability of $ZnCo_2O_4$ nanoparticles. The Fourier transform infrared spectrometer confirmed the functional group of $ZnCo_2O_4$ nanoparticles (FTIR). Cyclic voltammetry was used to quantify the specific capacitance 434 Fg^{-1} of $ZnCo_2O_4$ nanoparticles at a scan rate of 5mVs^{-1}. In addition, the high specific capacitance of $ZnCo_2O_4$ nanoparticles demonstrates desirable stability for supercapacitor applications.

[21] **Meenu Sharma et.al., (2019)** aimed to achieve good super capacitive performance, so they constructed Copper doped Zinc Cobalt oxides ($Zn_{1-x}Cu_xCo_2O_4$) nanostructures using a simple hydrothermal technique. Cu insertion into $ZnCo_2O_4$ results in a doubling of specific surface area (52 m^2g^{-1}) and a reduction in charge transfer resistance for the $Zn_{0.7}Cu_{0.3}Co_2O_4$ (x=0.3) sample. As a result, the Cu-doped $Zn_{0.7}Cu_{0.3}Co_2O_4$ electrode has a high specific capacitance of 1425 Fg^{-1} which is 1.55-fold higher than the pure $ZnCo_2O_4$ electrode's 917 Fg^{-1}. After 2000 charge-discharge cycles, the $Zn_{0.7}Cu_{0.3}Co_2O_4$ retains around 96% of its capacitance. Later, a solid-state symmetric supercapacitor made of $Zn_{0.7}Cu_{0.3}Co_2O_4$ that has an expanded cycle stability and a 1.5 V potential window has been created. The constructed device has a high energy density of 55 $Whkg^{-1}$ at a power density of 2621 WKg^{-1} and successfully illuminates the 1.5 V yellow LED. The enhanced surface area and electronic conductivity of the electrode are responsible for the significant improvement in electrochemical performance. The results demonstrated unequivocally that the constructed solid-state symmetric supercapacitor seems to have the ability to be utilized in flexible energy storage systems.

[22] **Loubna Merabet et.al., (2018)** agreed that the high-efficiency MCo_2O_4 spinels (M = Ni, Mn, Cu, Zn) were produced using the sol-gel technique (citrate), and their capacitive response in the alkaline electrolyte was explored. Employing cyclic voltammetry (CV) and electrochemical impedance spectroscopy, the capacitive characteristics of crystal MCo_2O_4 samples were fully examined in 1 M KOH aqueous electrolyte (EIS). The results demonstrated that the samples had great stability and outstanding electrochemical reversibility, as well as specific capacity based on the form of the transition metal ion M.

$CuCo_2O_4$ has a significant specific capacitance of 285 Fg^{-1} and $ZnCo_2O_4$ has a moderate capacitance of 158 F g^{-1}. Furthermore, MCo_2O_4 spinels displayed superior stability during long-term cycles, with a cycling performance above 75% after 1000 cycles. According to the findings, MCo_2O_4 cobaltite spinels are the most potential material for use in supercapacitors.

[23] **Juliet Christina Mary et.al., (2018)** generated $ZnCo_2O_4$ nanomaterials for supercapacitor applications utilizing three different methods: reflux, hydrothermal, and sol-gel. The material's electrochemical performance was investigated using a three-electrode system. The greatest specific capacitance of a $ZnCo_2O_4$ nanorod produced by reflux was 138 F g^{-1} at a scan rate of 5 mV s^{-1} and 126 F g^{-1} at a current density equal to 1.5 A g^{-1}. This finding indicated that $ZnCo_2O_4$ nanomaterial generated through the reflux process is acceptable for supercapacitor applications.

[24] **Zhiyong Gao et.al., (2018)** with a simple hydrothermal deposition and subsequent thermal annealing treatment, a $ZnCo_2O_4$-rGO composite with interwoven sheets grown onto a nickel foam substrate is created, which may be used directly as a binder-free electrode of a supercapacitor. An extremely high electrode specific capacitance (C_s) of 3222 Fg^{-1} at 1 Ag^{-1} in an alkali electrolyte is made possible by the hierarchically porous texture of $ZnCo_2O_4$-rGO composite, which has a large specific surface area and effective ions diffusion channels. The C_s still remain at 860 Fg^{-1} at 20 Ag^{-1}. The $ZnCo_2O_4$-rGO/activated carbon (AC) asymmetric supercapacitor can provide a maximum device specific capacitance (C_{cell}) of 139 F g^{-1} at 0.5 Ag^{-1} and consequently, an energy density (E_{cell}) of 49.1 $Whkg^{-1}$ at a power density (P_{cell}) of 400 Wkg^{-1} when utilized as the positive electrode of the whole cell. The asymmetric device can indeed maintain an E_{cell} of 18.8 Wh kg^{-1} even at a high P_{cell} of 7625 Wkg^{-1}. Most importantly, after 5000 charge-discharge cycles, the asymmetric supercapacitor shows just 6% C_{cell} fading. The faradic $ZnCo_2O_4$-rGO composite's balanced E_{cell}, P_{cell} delivery abilities, and high cyclability emphasize its potential in superior efficiency and extended lifetime energy storage devices.

[25] **Saravanakumar et.al., (2018)** prepared at three major hydrothermal process temperatures (100 °C, 130 °C, and 160 °C), urea is used to help in the synthesis of zinc cobalt oxide ($ZnCo_2O_4$) microspheres. $ZnCo_2O_4$ microspheres have a spinel face-centered cubic (Fd3m) structure, according to XRD measurements. For all three synthesized

products, the significant near band edge emission peak found at 392 nm corresponds to the straight recombination of the exciton-exciton collision process; SEM analysis indicates the whole growth stage of spherical $ZnCo_2O_4$ microspheres at three distinct temperatures. $ZnCo_2O_4$ microspheres (SH3-160 °C) have a higher specific capacitance of 500 F/g at 0.75 A/g current density and a specific capacitance of 80% at 2 A/g current density. For use as an electrode in supercapacitor applications, $ZnCo_2O_4$ microspheres (SH3-160 °C) would be a promising choice.

[26] **Vijayakumar et.al., (2018)** acknowledged that conventional hydrothermal process was used to create the Ni doped $ZnCo_2O_4$ mesoporous rods. Based on data from N_2 absorption isotherms, mesoporous rods of $Zn_{0.8}Ni_{0.2}Co_2O_4$ were discovered to have a surface area of 56 m^2g^{-1} and pore sizes of 10 nm. It is observed that the crystal structure's lattice parameter is 8.138 Å. XRD results reveal that the typical crystallite size is 12 nm, in general. The sample's phase formation temperature is 450 degrees, in accordance with a TGA investigation. As per research using electron microscopy, the mesoporous rods are composed of numerous crystalline nanoparticles. By using cyclic voltammetry (CV) and galvanostatic charge-discharge (GCD) experiments in a three-electrode setup with 6M KOH as the electrolyte, the sample's electrochemical characteristics were examined. With a scan rate of $2mVs^{-1}$, the working electrode's specific capacitance (Cs) was discovered to be 2021 Fg^{-1}. Besides that, GCD is used to evaluate the mesoporous rods electrochemical cycling stability at various current densities. It is concluded that the determined retention is 96% of its initial condition even after 1000 cycles, with a highest Cs of 628.75 Fg^{-1} at 2.5 Ag^{-1}.

[27] **Huiyu Chen et.al., (2018)** synthesized a simple two-step methodology that involves a solvothermal process in a water and ethanol solution combined with a following annealing process of the precursor in air that has effectively produced novel urchin-like $ZnCo_2O_4$ microstructures. With a specific surface area of 28 m^2 g^{-1}, these $ZnCo_2O_4$ microspheres resemble urchins and are made up of many porous nanorods with diameters ranging from 80 to 200 nm. By varying the volume ratios of water to ethanol, the forms of the resulting $ZnCo_2O_4$ samples can be efficiently adjusted. With a noteworthy cycling stability of 107.3% capacitance retention after 5000 cycles of charge-discharge operation at 5 A g^{-1} in KOH electrolyte (2 M), the unusual urchin-like $ZnCo_2O_4$ microsphere electrode offers a high specific capacitance of 677 F g^{-1} at 1 A g^{-1}. The increased

supercapacitor performance is most likely due to its mesoporous structure, which provides a high response surface area and quick ion/electronic transfer. It has a lot of potential as an improved electrode substance for extremely efficient electrochemical capacitors.

[28] **John Anthuvan Rajesh et.al., (2017)** made with a simple hydrothermal synthesis of hierarchical coral-like $ZnCo_2O_4$ nanostructures made of chain type nanowires that does not require the use of surfactants. The hierarchical coral structure is made up of a necklace-like nanowire arrangement on the nanoscale, which allows for charge transmission. Furthermore, the coral-like $ZnCo_2O_4$ nanowires were mesoporous (29.36m^2 g^{-1} and 18.96 nm), which resulted in extensive electrochemical active sites for the redox process and rapid ion transport within the $ZnCo_2O_4$ nanowires. Coral-like $ZnCo_2O_4$ nanowires showed outstanding cycling stability (capacitance retention of 85% even after 2000 cycles at a charge-discharge current density of 10 A g^{-1}), high rate capability (264 F g^{-1} at 10 A g^{-1}), and a very high specific capacity (694 Fg^{-1} at a current density of 2 A g^{-1}) when utilized in electrochemical supercapacitors of the interconnected necklace type. These findings show that hierarchical coral-like $ZnCo_2O_4$ nanowires are a suitable electrode material for high-performance pseudo capacitors.

[29] **Xuechun Xiao et.al., (2017)** prepared a simple hydrothermal technique and subsequent thermal annealing procedure to create the mesoporous $ZnCo_2O_4$ nanosheets. The sample was analyzed in order to learn about its crystal structure, shape, and BET surface area. In fact, nanosheets have a hexagonal shape with a mesoporous structure. The mesoporous $ZnCo_2O_4$ nanosheets produced have a significant specific surface area of 191.64 m^2/g. The $ZnCo_2O_4$ nanosheets exhibit good cycle stability in 6 mol/L KOH aqueous electrolyte with specific capacitance staying 73.28% of the initial value after 1000 continuous charge-discharge cycles at a current density of 8 A/g, as well as a high specific capacity of 835.26 F/g at the current density of 1.0 A/g. Their improved electrochemical properties show that mesoporous $ZnCo_2O_4$ nanosheets are a suitable electroactive material for supercapacitors.

[30] **Qichong Zhang et.al., (2017)** intended to discover a simple and low-cost method for directly growing three-dimensionally well-aligned zinc-nickel-cobalt oxide (ZNCO)@$Ni(OH)_2$ nanowire arrays (NWAs) on a carbon nanotube fiber (CNTF) with an ultrahigh specific capacitance of 2847.5 F/cm^3 (10.678 F/cm^2) at a current density of

1mA/cm^2. These levels are almost five times that of ZNCO NWAs/CNTF electrodes (2.10 F/cm^2) and four times that of $Ni(OH)^2$/CNTF electrodes (2.55 F/cm^2). The authors constructed a prototype coaxial FASC (CFASC) with a maximum operating voltage of 1.6 V using ZNCO@$Ni(OH)_2$ NWAs/CNTF as the crucial electrode and a thin carbon layer of coated vanadium nitride (VN@C) NWAs on a carbon nanotube strip (CNTS) as the outer electrode, with KOH poly(vinyl alcohol) (PVA) as the gel electrolyte. Our CFASC device attained a high specific capacitance of 94.67 F/cm^3 (573.75 mF/cm^2) and an excellent energy density of 33.66 mWh/cm^3 (204.02 μWh/cm^2), representing the greatest levels of fiber-shaped supercapacitors so far. In addition, the fiber-shaped ZnO-based photodetector exhibits remarkable sensitivity to UV light and is powered by the embedded CFASC. As a result, the research provides the door for the development of ultra-high capacity electrode materials for the upcoming generation of wearable energy storage systems.

[31] **Juliet Christina Mary et.al., (2017)** executed a hydrothermal approach to create Mn-doped $ZnCo_2O_4$ nanoparticles without the use of surfactants. The structural, morphological, and electrochemical properties of Mn-doped $ZnCo_2O_4$ nanoparticles at varied concentrations have been examined. The three-electrode system is used to measure the specific capacitance of the 10% Mn-doped $ZnCo_2O_4$ nanomaterial. With a current density of 0.5, 10 wt% Mn-doped $ZnCo_2O_4$ has a high capacitance of 707.4 F g^{-1}. For 500 cycles in the KOH electrolyte condition, the substance's Coulombic efficiency is 96.3%. A two-electrode device built of 10% Mn-doped $ZnCo_2O_4$ has the best specific capacitance of 6.5 F g^{-1} at a current density of 0.03 A g^{-1} and is therefore appropriate for supercapacitor applications.

[32] **Chun Wu et.al., (2015)** planned for the first time, nickel foam-based hierarchical mesoporous Zn-Ni-Co ternary oxide (ZNCO) nanowire arrays to produce using a simple strategy that includes a hydrothermal method and a following calcination step and is immediately used for super capacitive research. The nickel foam-based hierarchical mesoporous ZNCO nanowire arrays have an extremely high specific capacitance value of 2481.8 Fg^{-1} at 1 Ag^{-1} and a good rate capability with around 91.9% capacitance retention at 5 Ag^{-1}. Furthermore, by using the ZNCO electrode as the positive electrode and activated carbon as the negative electrode, a successful asymmetric supercapacitor with a large energy density (35.6 $Whkg^{-1}$) and exceptional cycle stability performance (94% capacitance retention over 3000 cycles) is created. The outstanding electrochemical

properties show that the nickel foam-assisted hierarchical mesoporous ZNCO nanowire array electrodes are ideal for use as improved supercapacitor electrodes.

[33] **Wenlong Bai et.al., (2015)** with a hydrothermal procedure and following calcination approach were used to create uniform $ZnCo_2O_4$ nanoflowers on a 3D layered structure of carbon nanotubes/nitrogen-doped graphene (NGN/CNTs) sheet. The $ZnCo_2O_4$ nanoflowers contain petals that are less than 100 nanometers wide and have a mean diameter of 4 m. With a high specific capacitance of 1802 F/g at 1 A/g and remarkable cycling stability (nearly 0% fade after 4000 sustained charge/discharge at 10 A/g), the as-synthetic $ZnCo_2O_4$/NGN/CNTs film may be employed directly as a flexible electrode. These findings indicate that the developed electrode has a promising future application in flexible energy modification systems. Furthermore, a binder-free asymmetric supercapacitor using $ZnCo_2O_4$/NGN/CNTs film as the positive electrode and NGN/CNTs film as the negative electrode has been created. This results in higher energy density (37.19 Wh/kg at 750 W/kg) and power density (14.992 kW/kg at 14.16 Wh/kg).

[34] **Jinbing Cheng et.al., (2015)** with a hydrothermal process, produced $ZnCo_2O_4$ nanoflakes on cellular nickel foam to serve as supercapacitor electrodes. The mesoporous $ZnCo_2O_4$ nanoflakes have large electroactive surface areas and good adherence to the Ni foam, allowing for rapid ion and electron transport. With a current density of 2 A g^{-1} in a 2 M KOH aqueous solution, the nanoarchitecture electrodes provide a good specific capacitance of 1220 F g^{-1} and long-term cyclic stability of 94.2% capacitance retention after 5000 cycles. The fabrication approach is simple and cheap, and it has considerable potential for massive supercapacitor applications.

[35] **Gang Zhou et.al., (2014)** used a straightforward electrospinning method, one-dimensional (1D) $ZnCo_2O_4$ porous nanotubes (PNTs) have been created. These PNTs were initially used in supercapacitors (SCs). The resulting $ZnCo_2O_4$ nanomaterial has a 1D geometry with extremely porous surfaces and hollow interiors. This novel structure increased the electroactive surface areas of $ZnCo_2O_4$, resulting in improved electrolyte/electrode interaction, more effective transport channels, and better strain accommodation. According to the findings of our experiments, it has a high specific capacitance of 770 F/g at 10 A/ g, a great rate property of 84% capacity retention at 60 A/ g, and remarkable cycling stability with just 10.5% loss after 3000 cycles. When compared to $ZnCo_2O_4$ nanoparticles, such developed PNTs have improved rates and capacitive

properties. Our findings show that as-prepared $ZnCo_2O_4$ PNTs can be used as advanced SCs materials. It is greatly anticipated that this easy electrospinning technology would be developed to manufacture similar superior electrochemical materials.

[36] **Marauo Davis et.al., (2012)** experimented $Zn(NO_3).6H_2O$ and $CoCl_2.6H_2O$ as precursors in the successful synthesis of highly crystalline Zinc cobaltite ($ZnCo_2O_4$) nanocrystals employing an epoxide-driven sol-gel technique. The generated nanocrystals have a diameter of 4 nm, based on the results. Electron microscope investigations show that changing the solvent and epoxide causes considerable changes. Gas sorption measurements reveal that the as-synthesized and warmed samples have large specific surface areas (>200 m^2 g^{-1}) and porosities. Experiments with cyclic voltammetry demonstrate that these Zinc cobaltite nanocrystals have remarkable capacitance (700 Fg^{-1}) and cycle endurance, which makes them a great electrode substance for supercapacitors.

[37] **Shubo Wang et.al., (2014)** made with a simple hydrothermal technique and subsequent thermal treatment step, uniform $ZnCo_2O_4$ nanowire arrays were directly produced on nickel foam. The $ZnCo_2O_4$ nanowires had lengths of up to 5 mm and diameters of approximately 100 nm. High-performance supercapacitors can use the nickel foam loaded with a $ZnCo_2O_4$ nanowire array that was generated directly as an electrode. The $ZnCo_2O_4$/nickel foam electrode has a significant specific capacitance (1625 F g^{-1} at 5 A g^{-1}), great rate capability (59% capacitance retention at 80 A g^{-1}), and excellent cyclic stability (94% capacitance retention over 5000 charge-discharge cycles), according to electrochemical studies. This study indicates that $ZnCo_2O_4$ nanowires are extremely attractive for use as advanced electrochemical electrode materials.

[38] **Bingkun Guan et.al., (2014)** with the aid of an easy hydrothermal technique, $ZnCo_2O_4$ nanowire cluster arrays (NWCAs) were grown directly on Ni foam. The $ZnCo_2O_4$ NWCAs on Ni foam were utilized directly as combined electrodes for supercapacitors and showed outstanding cycling ability at different current densities up to 100 mA cm^{-2}(40 A g^{-1}) and a large specific capacitance of 4.05 F cm^{-2} at 20 mA cm^{-2} (1620 F g^{-1} at 8 A g^{-1}) in 3 M KOH aqueous solution. 90% of the initial capacitance was still present over 6000 cycles. Asymmetric supercapacitors also have high energy densities of 41.00 W h kg^{-1} at a power density of 384 W kg^{-1} and 16.63 W h kg^{-1} at a substantial power density of 2561 W kg^{-1}. Because of their great rate qualities and excellent cycling life,

$ZnCo_2O_4$ NWCAs can be used not only in high energy density fields, but also in high power density applications.

[39] **Hao Wu et.al., (2014)** describe a facile and quick hydrothermal technique for producing $ZnCo_2O_4$ nanorods on a Ni wire as fiber electrodes. A two-electrode system was used to investigate the electrochemical properties of the free-standing supercapacitor. The specific capacitance of the supercapacitor was 10.9 F g^{-1}. The fiber supercapacitors also have an energy density of 76 mWh kg^{-1} and a power density of up to 1.9 W kg^{-1}. When bent at various angles, the flexible supercapacitor demonstrated outstanding electrochemical stability, demonstrating its potential for usage as electrodes for wearable energy storage.

[40] **Bin Liu et.al., (2013)** used a straightforward scalable solution method to create hierarchical $ZnCo_2O_4$/nickel foam designs. These architectures demonstrated extraordinary electrochemical behavior in supercapacitors with a significant specific capacitance (1400 F g^{-1} at 1 A g^{-1}), outstanding rate capability (72.5% capacity retention at 20 A g^{-1}), and good cycling stability (just 3% loss after 1000 cycles at 6 A g^{-1}). By joining two sections of the $ZnCo_2O_4$- based electrodes, all-solid-state supercapacitors have also been created, exhibiting outstanding results in terms of significant specific capacitance and long cycling stability. This research demonstrates that the as-prepared structures can be used in both great energy density fields and high-power density applications, including flexible electronics, electric cars, and energy storage devices.

2.2 Zinc cobaltite-based Lithium batteries:

[41] **Subashchandrabose Thoka et.al., (2020)** is interested in $LiCO_2$ batteries because of their high energy density and usage of the greenhouse gas CO_2 to produce energy. Although Li-CO_2 batteries have a number of drawbacks, the two most significant are their low cyclability and the large charge overpotential that is required to decompose the extremely insulating discharge product (Li_2CO_3). As a cathode material in Li-CO_2 batteries, spinel Zinc cobalt oxide porous nanorods with carbon nanotubes ($ZnCo_2O_4$@CNTs) composite is used in this study to enhance the cycling performance of the latter. When operated at a current density of 100 mA g^{-1} and a fixed capacity of 500 mAh g^{-1}, the $ZnCo_2O_4$@CNT cathode-based $LiCO_2$ battery demonstrated a full discharge capacity of 4275 mAh g^{-1} and outstanding cycling performance over 200 cycles with a

charge overpotential of less than 4.3 V. The synergistic effects of $ZnCo_2O_4$ and CNT were attributed to the better performance of the $ZnCo_2O_4$@CNT cathode composite. The extremely porous $ZnCo_2O_4$ nanorod architectures in the $ZnCo_2O_4$@CNT catalyst showed improved catalytic activity/stability, increasing CO_2 diffusion throughout the discharging process and accelerating Li_2CO_3 breakdown at low charge overpotential.

[42] **Lun Lu et.al., (2018)** worked with a simple pattern solvothermal approach and a following annealing procedure, mesoporous nanoring-like Zn-Co mixed oxides are created. The complexing effects of potassium sodium tartrate result in the formation of ring-like nanostructures having hollow interiors. During the precursor's 500 °C annealing, many mesopores are produced. The mesoporous nanoring-like Zn-Co mixed oxides, when used as anode materials, can attain an elevated discharge capacity of 1102 mAh g^{-1} over 200 cycles at 500 mA g^{-1}. The mixed oxides can still have a reversible capacity of 761 mAh g^{-1} despite the fact that the current density is raised to 2 A g^{-1}. This remarkable cycle stability and rate capability are primarily because of the distinctive mesoporous ring-like nanostructures and the synergistic impacts of Zn and Co-based oxides.

[43] **Mi-Hee Jung (2017)** used the solvothermal approach to convert two-dimensional (2D) nanosheets into three-dimensional (3D) microspheres in order to construct the transition structure of $ZnCo_2O_4$. The interaction of zinc acetate and cobalt nitrate in non-aqueous methanol resulted in $ZnCo_2O_4$ nano crystallites. Because of the directed attachment of $ZnCo_2O_4$ nano crystallites, a 2D wrinkled-paper-like structure of $ZnCo_2O_4$ is formed. Because there is no adequate surfactant and the precursor solution contains weak electrical double layers, the 2D $ZnCo_2O_4$ nanosheets agglomerate spontaneously. The aggregation of $ZnCo_2O_4$ nanosheets was changed into 3D $ZnCo_2O_4$ microspheres when the stacking of 2D $ZnCo_2O_4$ nanosheets increased. The $ZnCo_2O_4$ transition structure was made by connecting $ZnCo_2O_4$ nanoparticles, yielding in a porous structure to support the volume expansion of the $ZnCo_2O_4$ structure during the charge process. $ZnCo_2O_4$ transition structure has a significantly elevated specific capacity and excellent cycle performance. The transition structure of $ZnCo_2O_4$ demonstrated an exceptional initial discharge specific capacity of 2094 mA h g^{-1} at a current density of 100 mA g^{-1}. After 200 cycles, the discharge capacity remains constant at 1296.91 mA h g^{-1}. The average specific capacity remained at 606.88 mA hg^{-1} even though the current density increased to 2000 mA g^{-1}.

[44] **Xiaoyi Hou et.al., (2017)** prepared a simple hydrothermal synthesis and post-annealing treatment to create wrinkled-paper-like $ZnCo_2O_4$ nanoflakes. It has a large capacity, great cyclability, and extremely high rate performance as an anode for lithium-ion batteries. After 500 cycles, a reversible capacity of 1138 mAh g^{-1} at 1 A g^{-1} was found. The reversible capacity may recover to 1089 mAh g^{-1} at 0.2 A g^{-1} after being cycled at current densities ranging from 0.2 to 25.6 A g^{-1}. The wrinkled-paper-like $ZnCo_2O_4$ nanoflakes have been shown to be potential for use as futuristic energy storage units.

[45] **Yadav. A et.al., (2016)** studied the impact of transition metal Cr^{2+} ion as a Zn^{2+} dopant in $Mn_{0.5}Zn_{0.5}Co_2O_4$. Solid-state reaction was used to create co-doped $Mn_{0.5}Zn_{0.5-x}Cr_xCo_2O_4$ (x = 0, 0.3 and 0.5) cobaltites. The samples generated are polycrystalline single-phase cubic spinels with the space group Fd3m, according to X-ray powder diffraction (XRD) examination. Cr^{2+} doping led to a rise in the mean size of particles. Other structural indices, including as X-ray density, micro strain, and dislocation density, demonstrate an analogous decreasing tendency as Cr^{2+} rises. The parent material, $Mn_{0.5}Zn_{0.5}Co_2O_4$, exhibits a high permittivity of 10^5 and exhibits a significant drop with increasing Cr^{2+} doping. Increased doping of Cr^{2+} increases dielectric loss, limiting its technological value. AC conductivity has been discovered to rise with rising Cr^{2+} content at low frequency.

[46] **Qiang Wang et.al., (2015)** used a two-step process to create core-shell $Co_3O_4/ZnCo_2O_4$ coconut-like hollow spheres. Their reversible capacity as the anode of lithium-ion batteries reaches up to 1278 mAh g^{-1} at 0.1C rate and maintains at 1093 mAh g^{-1} after 50 cycles, which is substantially greater than pure Co_3O_4. Its reversible capacity can remain at 934 mAh g^{-1} at a 0.2C rate even after 300 cycles (cycling for more than 4 months). The distinctive core-shell hollow structure, complex synergistic effect, outstanding electrical conductivity, and interfacial charging mechanism are to blame for the superior electrochemical performance (high reversible capacity, great long-term cycling stability, and good rate capability). The evidence reported here shows that the hollow spheres with a core-shell composition of Co_3O_4 and $ZnCo_2O_4$ are potential anode materials for increased-performance lithium-ion batteries.

[47] **Guoxin Gao et.al., (2015)** The formation of ultrathin $ZnCo_2O_4$ nanosheets on reduced graphene oxide (denoted as $rGO/ZnCo_2O_4$) is described using a simple low-temperature solution approach followed by an annealing treatment. On both sides of the rGO sheets, interconnected $ZnCo_2O_4$ nanosheets can form hierarchically porous overlays with the help

of citrate. For reversible lithium storage, such a hybrid nanostructure would effectively facilitate charge transport and handle volume variation over lengthy charge/discharge cycling. The rGO/$ZnCo_2O_4$ nanocomposite exhibits a very stable high reversible capacity of about 960 mAh g^{-1} over 100 cycles at a low current density of 90 mA g^{-1} and outstanding rate capability.

[48] **Alok Kumar Rai et.al., (2014)** using a straightforward, low-temperature auto-combustion process supported by urea, $ZnCo_2O_4$/graphene, and pure $ZnCo_2O_4$ nanoparticles were created, which were then annealed at 400°C for 5 hours in an environment of air. The acquired $ZnCo_2O_4$/graphene nanocomposite electron microscopy image demonstrated that the $ZnCo_2O_4$ nanoparticles were randomly dispersed and attached on the surface of reduced graphene nanosheets. The $ZnCo_2O_4$ nanoparticle aggregation was controlled and the particle size was dramatically reduced by the graphene nanosheets, all while maintaining the sample's high electrical conductivity. The nanoparticles were 50-100 nm in size, while the nanoparticles in the nanocomposite sample were 25-50 nm in size. In comparison to pure $ZnCo_2O_4$ nanoparticles (299.8 mAh g^{-1} after 70 cycles and 302.4 mAh g^{-1} at 4.5 C), the electrochemical results showed that the $ZnCo_2O_4$/graphene nanocomposite electrode had much superior cycling stability. It had a high reversible capacity of 755.6 mAh g^{-1} after 70 cycles and a greater rate capability of 378.1 mAh g^{-1} at 4.5 C. The improved electrochemical performance of the nanocomposite could be attributed to the synergistic effect of $ZnCo_2O_4$ nanoparticles and conductive graphene nanosheets.

[49] **Haowen Liu et.al., (2013)** executed a hydrothermal process to initially create $ZnCo_2O_4$ nanorods. According to the findings, the diameter and length of as-produced $ZnCo_2O_4$ nanorods are between 15 and 22 nm and 150 to 200 nm, etc. On the initial cyclic voltammogram curve, two cathode peaks had never been seen together before. A nanorod manufacturing mechanism and a charge-discharge mechanism have also been proposed. According to EIS measurements, $ZnCo_2O_4$ nanorods have a reduced surface layer resistance (192Ω), that can enhance electrochemical activity. Clearer plateaus may be seen at 0.5 V for the first discharge curve and 0.05 V for all discharge curves. 1509 mAh g^{-1} is the initial discharge capacity. The capacity after 50 cycles is 767.15 mAh g^{-1}. The $ZnCo_2O_4$ nanorods that were produced have excellent potential for use as lithium ion battery anode materials.

[50] **Lingling Hu et.al., (2013)** in a study, a straightforward ethylene glycol (EG) assisted solvothermal technique was used to successfully generate three-dimensional (3D) uniform ZnCo-glycolate precursor microspheres made of nanosheets. They might be transformed into homogeneous mesoporous $ZnCo_2O_4$ microspheres with encircling nanoparticles by moderately calcining the as-produced ZnCo-glycolate precursor. The outcomes showed that Li-ion batteries surface texture and pore size tuning of $ZnCo_2O_4$ products were extremely significant (LIBs). The uniform mesoporous $ZnCo_2O_4$ microspheres have improved cycling performance, higher rate capability, and excellent high specific capacity. The homogeneous mesoporous $ZnCo_2O_4$ microspheres demonstrated a high initial specific capacity of 1332 mAh g^{-1} at a current density of 100 mA g^{-1}. After 80 discharge-charge cycles, the capacity remained constant at 721 mAh g^{-1}. The initial specific capacity remained at 937 mAh g^{-1}, and the discharge capacity of 432 mAh g^{-1} was sustained after 40 cycles, even when the current density reached 1000 mA g^{-1}.

[51] **Bin Liu et.al., (2012)** created high-performance binder-free anodes for Li-ion batteries, hierarchical three-dimensional $ZnCo_2O_4$ nanowire arrays/carbon cloth composites. These composites have a capacity of 1200 mAh g^{-1} and excellent cycling ability even after 160 cycles. They also have a high reversible capacity of 1300–1400 mAh g^{-1}. Moreover, highly flexible complete batteries were created, showing better electrochemical performance, great electrical stability, and high flexibility.

[52] **Wei Luo et.al., (2012)** made porous $ZnCo_2O_4$ nanotubes using a simple single-nozzle electrospinning technique and subsequent heating. The polycrystalline $ZnCo_2O_4$ nanotubes have lengths up to many millimeters and diameters between 200 and 300 nm. The walls are 50 nm thick and contain many nanopores (3 nm) and connected $ZnCo_2O_4$ nanocrystals (30 nm). The resultant $ZnCo_2O_4$ nanotubes demonstrate remarkable electrochemical lithium-storage characteristics with a high specific capacity, strong cyclability, and great rate capability when tested as an anode material for lithium-ion batteries. A good anode choice for lithium-ion batteries is demonstrated by the high reversible capacity of 1454 mAh g^{-1} at 100 mA g^{-1}, which even increases to 794 mAh g^{-1} at a current density as high as 2000 mA g^{-1} after 30 discharge/charge cycles.

[53] **Yongcai Qiu et.al., (2010)** presents the effective synthesis of unique hexagonally structured, highly ordered, inorganic-organic-inorganic layered hybrid nano disks through morphology preservation and pyrolysis-induced transformation into porous $ZnCo_2O_4$

nanoflakes. It is demonstrated that the hexagonal hybrid nano disks are made of inorganic bilayers assembled under the control of an organic molecule (ethylene glycol). Many structural and spectroscopic approaches have been used to establish the assembly mechanism. In studies as a lithium ion battery electrode, the porous $ZnCo_2O_4$ nanoflakes demonstrated good capacity and great cyclability.

[54] **Xiuhua Wei et.al., (2007)** researched the thermal degradation of Zn-Co gel made by sol-gel technique with oxalic acid as a chelating agent yielded the Zinc-cobalt-oxide spinel. After calcination at 350 °C, it was discovered that a perfectly crystallized spinel structure is created (low-temperature spinel). The particle size of 15 - 20 nm was determined using a transmission electron microscopy (TEM). At low temperatures, the spinel compound $ZnCo_2O_4$ can be produced using the practical and efficient sol-gel technique.

Less studies are made for Lithium batteries in which Dysprosium and Lanthanum (i.e. the rare earth elements) as dopants are not yet reported. Electrochemical performance evaluation with Chromium is not completely understood so far.

Table 3.1 Electrochemical performances of Zinc cobaltite-based supercapacitors, Lithium batteries

AUTHOR & YEAR	METHOD	ELECTROCHEMICAL PERFORMANCE	REFERENCES
Changchun ai et.al., (2003)	Hydrothermal method	Initial discharge capacity is 1320 mAh/g with a large irreversible capacity about 612 mAh/g. Current density is 100 mA/g. Cyclic performance of 95% is observed.	[55]
Yogesh Sharma et.al., (2007)	Urea Combustion method	Stable cycling performance in the range 5–60 cycles at 60 mAg^{-1} and at 25 °C with ~ 98% coulombic efficiency. It yields a reversible capacity of 900 and 960 mAh g^{-1}.	[56]

Reddy et.al., (2011)	Molten salt method	$ZnCo_2O_4$ showed a high and stable capacity of 974mAhg^{-1} at the end of 40th cycle, at current rate of 60 mA g^{-1} and voltage range of 0.005V–3.0 V.	[57]
Ning Du et.al., (2011)	Microemulsion method	The specific surface areas of $ZnCo_2O_4$ nanowires (500°C) and $ZnCo_2O_4$ nanowires (700°C) are 68.86 m^2 g^{-1} and 35.99 m^2 g^{-1}. The reversible capacity of $ZnCo_2O_4$ nanowires synthesized at 500°C is maintained at 1197 mA h/g.	[58]
Beihong Liu et.al., (2012)	Facile fast co-ordinating etching and a thermal process	$ZnCo_2O_4$ has a high reversible discharge capacity of 1025 mAhg^{-1} at 500 mAg^{-1} after 200 cycles, and outstanding rate capability of 525 mAhg^{-1} at 4 Ag^{-1}.	[59]
Zhipeng Sun et.al., (2014)	Hydrothermal method combined with a chemical bath deposition method	ZCO/NiO NWs also exhibit a high specific surface area of 119.9m^2 g^{-1}. ZCO NWs with the current density increasing from 0.2 A g^{-1} to 0.8 A g^{-1}.	[60]
Peng Yuan et.al., (2014)	Facile solvothermal method	Ni foam-supported Zn–Co hydroxide nanoflakes exhibited a high specific capacitance of 901 F g^{-1} at 5 A g^{-1} and excellent cycling stability. Zn–Co hydroxide electrode after charging–discharging for 1000 cycles at a current density of 5 A g^{-1}.	[61]
Satyajit Ratha et.al., (2014)	Hydrothermal method	The work function of $ZnCo_2O_4$ micro flower is 5.22 eV and a current density of 0.01 mA cm^{-2}.	[62]
		At a current density of 100 mAg^{-1}, it shows an excellent initial specific capacity	[63]

Arnab Kanti Giri et.al., (2014)	Hydrothermal method	of 527 $mAhg^{-1}$, which is maintained up to 50 cycles.	
Jing Bai et.al., (2014)	Polyol method and thermal treatment	The samples of $ZnCo_2O_4$ twin microspheres and microcubes deliver the capacity of discharge 1145 and 1045.3 mA h g^{-1}.	[64]
Youqi Zhu et.al., (2015)	Microwave-assisted liquid phase growth and a post annealing treatment	$ZnCo_2O_4$ nanosheets exhibit high initial discharge–charge capacities of 1310.9 and 1086.8 mA h g^{-1} at 200 mA g^{-1}. After 200 repeat cycles, the reversible capacity is retained at 956.2 mA h g^{-1}.	[65]
Hao Niu et.al., (2015)	Hydrothermal method followed by thermal treatment	PCF@$ZnCo_2O_4$ electrode could achieve a high capacitance of 1384 F g^{-1} at a scan rate of 2 mV s^{-1}. PCFs as negative electrode achieves a high energy density of 49.5 $Whkg^{-1}$ at a power density of 222.7 W kg^{-1}.	[66]
Xiaoli Ge et.al., (2015)	Hydrothermal method	ZnO/$ZnCo_2O_4$/C hybrid Lithium-ion batteries anodes can maintain a specific capacity of 669 $mAhg^{-1}$ after 250 cycles under a current density of 0.5 mA g^{-1}.	[67]
Bin Liu et.al., (2015)	Hydrothermal method	The ZCO/SWCNT composite electrode possesses a more stable cycling capability, higher reversible capacity 1500 $mAhg^{-1}$ at the 10th cycle with a current density of 0.1 $mAcm^{-2}$.	[68]
Yue Pan et.al., (2016)	Hydrothermal method	The initial lithiation-specific capacity of $ZnCo_2O_4$ NCPs with a current density of 100 mA g^{-1} reached 1110 $mAhg^{-1}$ with a coulombic efficiency of 98.9 %.	[69]

Qiaobao Zhang (2016)	Chemical bath deposition method and annealing treatment	ZNCO/GNS core/shell composite electrode exhibited superior lithium storage performance in terms of high specific capacity (1015 $mAhg^{-1}$ at 0.1C after 50 cycles), outstanding cycling stability (420 $mAhg^{-1}$ after 900 cycles at rate of 1 C), and good rate capability.	[70]
Gracita Tomboc et.al., (2016)	Hydrothermal method	$ZnCo_2O_4$ NPs with ring-like morphology (P2) showed the highest specific capacitance of 2834.18 F g^{-1} at a scan rate of 2 mVs^{-1} and displayed excellent cycling ability even after 3000 cycles at 50 mV s^{-1} scan rate.	[71]
Hitesh Adhikari et.al., (2016)	Hydrothermal method	Specific surface of $ZnCo_2O_4$ is 29.47 m^2/g with a specific capacitance of 66.50 at a current density of 3 A/g. At an energy density of 2.95 Wh/kg, power density of 1455.30 W/kg is observed.	[72]
SubbukalaiVijaya kumar et.al., (2016)	Hydrothermal method	A maximum specific capacity of 886 Cg^{-1} at a current density of 2 $mAcm^{-2}$. $ZnCo_2O_4$ suggest that the prepared electrode is a promising candidate for hybrid supercapacitor applications.	[73]
In Kyu Moon et.al., (2016)	Chemical bath deposition method	$ZnCo_2O_4$/rGO/sponge electrode yields the highest specific capacitance which is 1116.6 Fg^{-1}. It shows excellent electrochemical performances with a specific capacitance of 143 Fg^{-1} at a current density of 1 Ag^{-1}.	[74]
Yisi Liu et.al., (2017)	Facile hydrothermal-calcination	ZnO/$ZnCo_2O_4$/C@rGO cathode displays higher specific capacity of 42.6 $mAhg^{-1}$, higher power density of 1.41 $mWcm^{-2}$ than those of the coin cell with	[75]

		$ZnO/ZnCo_2O_4$/C cathode, constant current density of 1.0 mA cm^{-2}.	
Swati J Patil et.al., (2017)	Facial one-step hydrothermal method on a carbon cloth	$ZnCo_2O_4$ microstrips electrode exhibited the highest specific capacitance of 1084 F/g at 2 mV/s scan rate. Maximum energy density of 12.5 Wh/kg was attained at a current density of 2 mA/cm^2 with the power density of 3.6 kW/kg.	[76]
A. Juliet Christina Mary et.al., (2017)	Graphene Oxide (GO) - Modified Hummers & Hoffman's method. $ZnCo_2O_4$ - Hydrothermal method.	The highest specific capacitance value of the composite material is 704.2 F/g at a current density of 0.75 A/g. Stability of $ZnCo_2O_4$/rGO nanocomposite was tested up to 400 cycles.	[77]
Saad G. Mohamed et.al., (2017)	Hydrothermal method	Exhibited high specific capacitance of 1596 F g^{-1} at 1 A g^{-1} and outstanding cycling stability of 119% after 2000 cycles. At a current density of 10 A g^{-1}.	[78]
Fatin Saiha Omar et.al., (2017)	Hydrothermal method	Enhanced specific capacity of 398 C/g at a current density of 1 A/g. High energy density (13.25 Wh/kg at 375 W/kg).	[79]
Xiong-Wen (David) Lou (2017)	Hydrothermal method	The obtained double-shelled Zn-Co-S RDCs exhibit enhanced performance with high specific capacitance (1266 F g^{-1} at 1 A g^{-1}),	[80]
Buddha Deka Boruah et.al., (2017)	Chemical Vapour Deposition method	Novel heterostructure is fabricated by combining electrochemically and optically active materials for high capacitive response of 896 F/g at 5 A/g.	[81]

Le Xu et.al., (2017)	Hydrothermal method	$ZnCo_2O_4$ nanostructures with high specific capacitance of 776.2 F g^{-1} at 1 A g^{-1} displays superior electrochemical performance with an ultrahigh energy density (84.48 Wh kg^{-1} at 0.4 kW kg^{-1}).	[82]
Haowen Liu et.al., (2018)	Hydrothermal method	Initial discharge capacity – 1307.8 $mAhg^{-1}$ at 0.1C. Coulombic efficiency was 99%.	[83]
A. Juliet Christina Mary et.al., (2018)	Hydrothermal method	The highest specific capacitance is 290.5 Fg^{-1} at a current density of 0.5 Ag^{-1}. The obtained maximum energy density is 0.469 $Whkg^{-1}$.	[84]
Ya Xiong et.al., (2018)	Hydrothermal method	The $ZnCo_2O_4$ yolk-shell spheres have a specific surface area of 74.8823 m^2/g with a pore volume of 0.2885 cm^3/g.	[85]
Jai Bhagwan et.al., (2019)	Co-precipitation method	The MWCNT@ZCO showed a specific capacity of 64 mAh g^{-1} at 1 A g^{-1}. 95% retention in the capacity was obtained till 1000 cycles.	[86]
Yujing Yang et.al., (2020)	Hydrothermal method	It delivers a high specific capacity of 214.1C g^{-1} (522 F/g) at the current density of 0.5 A g^{-1}, S-$ZnCo_2O_4$ also shows good rate capability (82% at 10 A g^{-1}).	[87]
A. Juliet Christina Mary et.al., (2020)	Hydrothermal method	rGO/$NiCo_2O_4$@$ZnCo_2O_4$ (RNZC) exhibits the maximum specific capacity of 1197 C g^{-1} at a current density of 1Ag^{-1}. RNZC3//rGO asymmetric supercapacitor device reaches the highest energy density of 71 W h kg^{-1} and the corresponding power density is 0.98 kW kg^{-1}.	[88]
Zixin Dai et.al., (2020)	Electro spinning, In situ growth,	High discharge specific capacity of 1707 mAh·g^{-1} in the initial cycle, superior cycle stability with a capacity of 1145 mAh·g^{-1}.	[89]

	Hydrothermal method		
G.P.Kamble et.al., (2021)	Reflux condensation method	The specific capacitance of the $ZnCo_2O_4$ electrode is calculated to be 315 F g^{-1} at a current density of 2 $mAcm^{-2}$.	[90]
Zixin Dai et.al., (2021)	Electro spinning, In situ growth, Hydrothermal method	A large discharge capacity of 2468 mAh g^{-1} was obtained at a current density of 0.1 A g^{-1} in the 1st cycle, also have an improved specific surface area (90.61 m^2 g^{-1})	[91]
Noor Hussien AbdAli et.al., (2021)	Hydrothermal method	A promising capacitance (1242 F g^{-1}) at a current density of 2 A g^{-1}). The device showed the highest energy density of 32Wh kg^{-1} at a power density of 1252 W kg^{-1}.	[92]

CHAPTER III

MATERIALS AND METHODOLOGY

3.1 Introduction:

This chapter deals with the experimental techniques used in the preparation and characterization of Cr, La, Dy doped Zinc cobaltite. The method employed for the synthesis of Zinc cobaltite is the Sol-gel method. The experimental techniques employed to understand the properties of the prepared materials are as follows:

- X-ray Diffraction (XRD)
- Electrochemical Characterization

3.2 Synthesis Techniques:

The general preparation methods for Zinc cobaltite is achieved are mentioned below.

- Sol-Gel method
- Hydrothermal method
- Co-precipitation method
- Polyol Process
- Solid State Reaction
- Combustion process

3.3 Sol-gel method:

Sol-gel preparation is a common technique for creating nanoparticles. Using chelating agents, the products in the sol-gel process are transformed into colloids. When processing the gel-like solution at a specific temperature, the powder is created. While preserving the pH level of the solution, this method of preparation offers benefits like controlled morphology, particle size, and microstructure. As a result, even little adjustments to the reaction process could have a significant effect on the final products' characteristics. Systems with high melting points benefit most from this strategy. [93]

The chemical reactions during general sol-gel processing can be formally described by two processes.

- ✓ Hydrolysis
- ✓ Condensation

When a continuous three-dimensional network is created, the sol-gel transition (gel point) is attained. The rate of gel formation increases with the rate of condensation processes. The initial reaction conditions used have a significant impact on the ultimate network structure, whether it be polymeric or colloidal. A particularly important aspect of the manufacture of inorganic gels by sol-gel processing is the realization that the chemical reactions do not come to an end with the creation of the solid network. Condensable particles are still present in the pore liquid, and the gel network may undergo structural changes (Ostwald ripening, syneresis). As a result, the gel must mature for a specific amount of period until it can be dried.

In the gel state, reaction rates and physical changes slow down, yet the system is still dynamic. This is clearly demonstrated by the syneresis, or contraction of the gel body when the solvent is ejected from the gel. Controlling the aging duration is crucial since syneresis and other processes can greatly affect the porosity and texture of the resultant gels. The drying of the wet gel structure completes the sol-gel manufacturing process. Here, a variety of paths can be taken: Traditional vacuum drying of the sample usually causes a significant contraction of the gel network. Surface modification or supercritical drying, which allows access to porous gels.

3.3.1 Advantages of the Sol-gel method:

Sol–Gel method offers several advantages, which are listed below.

- The sol-gel technique is easier and less expensive than others.
- It can easily coat large and complex-shaped substrates (if the angles are not too sharp),
- The process is cost-effective in terms of the initial investment in the production plant and the running cost.
- It doesn't cause any disruption to devices when the deposition is applied on top.

- It provides simple control of film thickness and porosity.
- It can produce ultrafine films.
- The significant surface area may be achieved on the films and powders to improve their properties.
- It is a low-temperature method.
- The technique may be simple to scale up.
- It can easily adjust the composition with evenly dispersed dopants and/or modifiers to improve the sensitivity and selectivity towards particular gas species. [94]

3.3.2 Disadvantages of the Sol-gel method:

- The procedure takes time and may involve several steps.
- The method is only applicable to specific substances, like silicates.
- It can be challenging to properly manage the manufactured material's qualities.
- The process must be scaled up for large-scale production, which is challenging.
- The environment, including factors like temperature and humidity, has a big impact on the process.
- Materials made of sol-gel can be fragile and challenging to handle.

3.4 Experimental Details:

3.4.1 Cr-doped in Zinc cobaltite:

Chromium is a chemical element with the atomic number 24 and the symbol Cr. It is the group 6's first element. Chromium exists in a series of oxidation states from -2 to +6 valence. The most important stable states are 0 (elemental metal), +3 (trivalent), and +6 (hexavalent). It is a transition metal that is steely grey, glossy, tough, and brittle. The great corrosion resistance and hardness of chromium metal make it valuable. Steel is hardened using chromium, which is also used to make stainless steel (so-called because it won't rust),

and a number of alloys. Chromium doped with Zinc cobaltite is prepared through Sol–gel method.

3.4.1.1 Raw materials used:

- Zinc chloride dry
- Cobalt (II) chloride hexahydrate
- Citric acid monohydrate
- Chromium (III) chloride

3.4.1.2 Preparation of Chromium doped Zinc cobaltite:

A 0.8 M solution of Zinc chloride anhydrous, a 0.2 M Chromium chloride, and 2 M solution of Cobalt chloride hexahydrate ($CoCl_2.6H_2O$) are weighed and mixed together in distilled water. The 1.33 M Citric acid solution is made, added, and continuously stirred into the chloride solution until all the salts are completely dissolved. The end product is heated for 6 hours at 80° C to produce a gel, followed by 5 hours at 550° C for calcination, after which the powder is collected for further analysis.

3.4.2 La-doped in Zinc cobaltite:

The chemical element lanthanum has the atomic number 57 and the symbol La. Lanthanides have a stable and common oxidation state of +3. It is a silvery-white, ductile, soft metal that slowly tarnishes when exposed to air. It serves as the lanthanide series eponym. Lanthanum is a prototype. The rare earth elements traditionally include lanthanum. Although some compounds are known to have an oxidation state of +2, like the majority of other rare earth elements, the typical oxidation state is +3. Although it plays no biological role in humans, some bacteria require lanthanum to survive. Although it doesn't pose a significant threat to humans, it does have some antimicrobial properties. Lanthanum doped with Zinc cobaltite is prepared through the facile Sol–gel method.

3.4.2.1 Raw materials used:

- Zinc chloride dry
- Cobalt (II) chloride hexahydrate
- Citric acid monohydrate
- Lanthanum (III) nitrate

3.4.2.2 Preparation of Lanthanum doped with Zinc cobaltite:

- 0.3 M solution of Zinc chloride dry ($ZnCl_2$), 0.2 M solution of Lanthanum nitrate and 1 M solution of Cobalt chloride hexahydrate ($CoCl_2.6H_2O$) are prepared and mixed together.
- The 0.665 M Citric acid is prepared and poured into the already prepared chloride solution under continuous stirring until all the salts get dissolved entirely.
- The resultant solution is heated at 150°C for 6h to achieve the gel formation and then calcined at 550°C for 5h after which the powder is collected for analysis. All the preparations are made using distilled water.

3.4.3 Dy doped in Zinc cobaltite:

The chemical element with the atomic number 66 and symbol Dy is called dysprosium. It is a lanthanide rare-earth element with a metallic silver luster. Although it is present in a variety of minerals, including xenotime, dysprosium is never found in nature as a free element. Seven isotopes make up naturally occurring dysprosium, the most prevalent of which is ^{164}Dy. Chemically, dysprosium behaves as a typical trivalent rare earth and forms a series of pale-yellow compounds in which an oxidation state is +3. Dysprosium doped with Zinc cobaltite is prepared through Sol–gel method.

3.4.3.1 Raw materials used:

- Zinc chloride dry
- Cobalt chloride Hexahydrate
- Citric acid monohydrate
- Dysprosium chloride

3.4.3.2 Preparation of Dysprosium doped with Zinc Cobaltite:

- The following solutions are made and combined: 0.3 M solution of dry Zinc chloride ($ZnCl_2$), 0.2 M solution of Dysprosium chloride tetrahydrate, and 1 M solution of Cobalt chloride ($CoCl_2.6H_2O$).

- The chloride solution is already prepared, and 0.665 M Citric acid is added while stirring continuously until all the salts are completely dissolved.

- The end product is heated for 6 hours at 150°C to produce a gel, followed by 5 hours at 550°C for calcination, following which the resulting powder is gathered for analysis.

3.5 Characterization Techniques:

The characterization techniques used for the analysis of the prepared samples are X-ray diffraction (XRD) and Cyclic Voltammetry (CV) to determine the structure and electrochemical performance of the materials synthesized. The electrochemical performance of the synthesized samples is evaluated utilizing Biologic SP-150 electrochemical workstation.

3.5.1 X-ray diffraction:

One of the most popular techniques is X-ray diffraction (XRD), which can be used to determine the crystalline or amorphous phase of a powder sample as well as to estimate various phase parameters like lattice constants, stress measurements, phase compositions, crystallite size, and defect structure. Using a X ray diffractometer, all of the generated samples' XRD patterns were captured between 10 to 80 degrees using Cu-K_α radiation (30 mA, and 40 kV). The ray diagram illustrating the X-Ray diffraction principle is displayed in Figure 2.1. Each sample's phase is determined by comparing the measured XRD pattern to the JCPDS data.

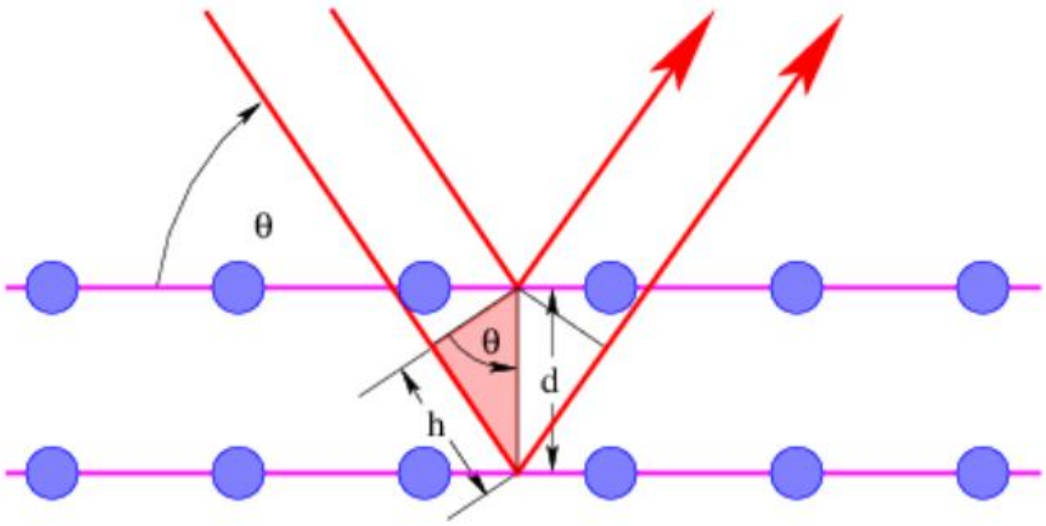

Fig 3.1 Ray diagram of X-Ray diffraction

The generation of X-ray electromagnetic waves results from the interaction of high-energy electrons with a copper (Cu) target (8.05 keV, 1.54 A).4 These X-rays interact with the interior structure of the crystal when they are irradiated on surfaces. When the incident beam makes contact with the crystalline plane at an angle of θ, constructive interference happens. Based on Bragg's law, the detector detects a series of interference signals coming from different directions θ, which corresponds to the lattice spacing:

$$n\lambda = 2d \sin\theta$$

where,

d = the distance between two atomic planes (lattice spacing),

n = an integer called the order of reflectance,

λ = the wavelength of the electromagnetic radiation, and

θ = the angle between the incident beam and normal to the reflecting crystalline plane.

The lattice spacing (d) is used to identify crystal structure and atomic composition. For crystallite sizes less than about 1μ m, destructive interference in the scattering direction takes place due to a shortage of long-range order in the crystal structure.

The diffracted peaks in XRD patterns are typically not always sharp; instead, they may be widened due to experimental conditions and/or the nature of the sample (mostly crystallite size). The peaks in the XRD pattern broaden more than typical when the sample's crystallite size decreases. X-ray line broadening data can be used to determine the average crystallite size of the particles. Using Scherrer's formula, the measured full width at half maximum (FWHM) peak intensity of the X-ray line broadening is used to calculate the sample's crystallite size.

$$D = \frac{k\lambda}{\beta \cos\theta}$$

where,

D indicates crystallite size,

k is the Scherrer constant.

λ is the x-ray wavelength, and

β is the obtained value of FWHM.

3.5.1.1 Instrumentation of X ray Diffraction:

X-ray diffractometers consist of three basic elements: An X-ray tube, a sample holder, and an X-ray detector. X-rays are generated in a cathode ray tube by heating a filament to produce electrons, accelerating the electrons toward a target by applying a voltage, and bombarding the target material with electrons. When electrons have sufficient energy to dislodge inner shell electrons to the target material, characteristic X-ray spectra are produced. These spectra consist of several components, the most common being Kα and Kβ. Kα consists, in part, of Kα1 and Kα2. Kα1 has a slightly shorter wavelength and twice the intensity as Kα2. The specific wavelengths are characteristic of the target material. Filtering, by foils or crystal monochromators, is required to produce monochromators, is required to produce monochromatic X-rays needed for diffraction. Kα1 and Kα2 are sufficiently close in wavelength such that a weighted average of the two is used. Copper is the most common target material for single-crystal diffraction, with Cu Kα radiation = 1.5406Å. These X-rays are collimated and directed onto the sample. As the sample and detector are rotated, the intensity of the reflected X-rays is recorded. When the geometry of the incident X-rays impinging the sample satisfies the Bragg Equation, constructive interference occurs and a peak in intensity occurs. A detector records and processes this X-ray signal and converts the signal to a count rate which is then output to a device such as a printer or a computer monitor. The geometry of an X-ray diffractometer is such that the sample rotates in the path of the collimated X-ray beam at an angle θ while the X-ray detector is mounted on an arm to collect the diffracted X-rays and rotates at an angle of 2θ. The instrument used to maintain the angle and rotate the sample is termed a goniometer. For typical powder patterns, data is collected at 2θ from 10° to 90°, angles that are preset in the X-ray scan. [95]

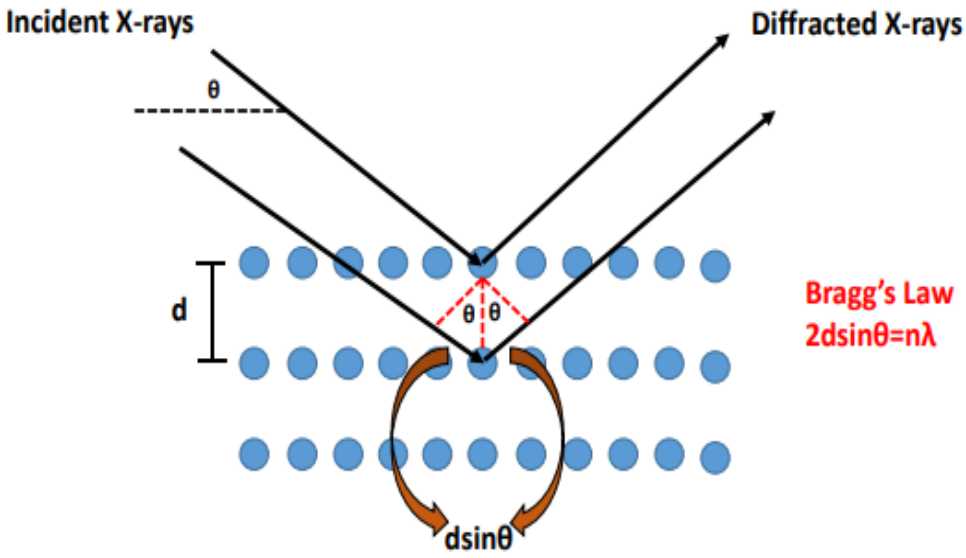

Fig 3.2 X- Ray Diffraction

Fig 3.3 Powder X-Ray Diffractometer

3.5.1.2 Applications of X-ray diffraction:

X-ray powder diffraction is most widely used for the identification of unknown crystalline materials. The determination of unknown solids is critical to studies in geology, environmental science, material science, engineering, and biology. Other applications include:

- ❖ Characterization of crystalline materials
- ❖ Determination of unit cell dimensions
- ❖ Measurement of sample purity

- ❖ Identification of the fine-grained minerals such as clays and mixed layer clays that are difficult to determine optically
- ❖ Determining dislocation density.

3.5.2 Electrochemical Characterization:

For the electrochemical characterization, a variety of tools and approaches have been created. Two of the most often used techniques are galvanostatic charge/discharge (GCD) testing and cyclic voltammetry (CV). Voltage, current, and time are the three basic parameters that are measured by both methods, and extra metrics like capacitance can be computed from them. A three-electrode configuration consisting of a working electrode, counter electrode, and reference electrode is used for basic analysis. A functioning electrode's performance can be evaluated using a three-electrode arrangement. The working electrode's potential is kept constant during the experiment by the reference electrode. The counter electrode completes the circuit without interfering with the working electrode's response. [96]

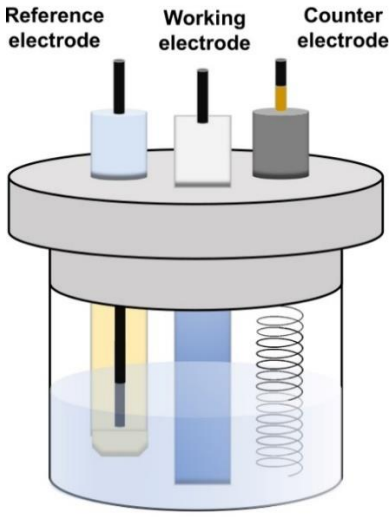

Fig. 3.3 Three-electrode arrangement

3.5.2.1 Cyclic Voltammetry (CV):

The potential is applied in cyclic voltammetry analysis between two operational potentials or potential windows on the working electrode. At a constant scan rate, the potential of the working electrode is swept. During positive and negative scans, the amount of current produced in the electrochemical system is measured as a function of the applied

voltage. The shape of the CV profile is thought to be responsible for the mechanism of energy storage at the electrode/electrolyte interface. Given a linear change in potential, ideal capacitors have a distinctive rectangular shape. Reversible redox processes in batteries cause faradaic peaks to appear on the voltammogram. Pseudo-capacitors have a quasi-rectangular form as a result of the presence of redox peaks. [97]

3.5.2.2 Specific Capacitance:

The specific capacity of an electrode is defined as the capability of the electrode to deliver current over a period of time. The value of specific capacity depends on the materials. The unit of capacity of the electrode is expressed as in terms of ampere-hour (Ah) or milliampere-hour (mAh). The calculation of the theoretical capacity per gram of the electrode material is expressed as given below;

The specific capacitance of a material is calculated from CV using the formula:

$$\mathbf{C} = \int \frac{\boldsymbol{I\,dv}}{\boldsymbol{vmV}} \quad \mathbf{F\ g^{-1}}$$

where,

$\int I\,dv$ – Integral area of the curve (A.V),

v – Scan rate (mV/s),

m - mass of the active material (g),

V - potential window (V).

3.5.2.3 Diffusion Coefficient:

An essential physical characteristic of the species involved in an electrochemical reaction that describes diffusional transport is the diffusion coefficient D.

$$\mathbf{D} = \left(\frac{\boldsymbol{B}}{\mathbf{2.69\times10^{5}}\ \boldsymbol{A\ Cn^{3/2}}}\right)^{2}$$

where,

B - Slope of the linear plot (mole/second)

A - Area of the electrode $(cm)^2$

C - Concentration of electrolyte (mole/ liter).

3.5.2.4 Applications of Cyclic Voltammetry:

CV has become a very popular technique for electrochemical studies of new systems, and has proved as a sensitive tool for obtaining information about fairly complicated electrode reactions. CV methods have found to have extensive applications for the evaluation of thermodynamic and kinetic parameters such as number of electrons change (n), heterogeneous rate constant (k_o), entropy (S), Gibb's free energy (G) and diffusion coefficient (D_o) etc., of a number of redox reactions and associated chemical reactions. These methods are especially useful in both oxidation and reduction process and to study the multiple electron transfer in an electrochemical reaction. Voltammetric detectors may also find increasing applications in chromatography.

Still research for these trivalent dopants are not reported in the literature and hence they are studied here.

CHAPTER IV

RESULTS AND DISCUSSION

4.1 STRUCTURAL CHARACTERIZATION:

4.1.1 XRD Analysis of Chromium doped in Zinc cobaltite:

The crystal structure of Zinc cobaltite with dopants was analyzed by powder X-ray diffraction technique (X-Pert Pro, PANalytical) using Cu-Kα radiation (λ= 1.5406 Å) at room temperature to determine the phase formation. The diffraction peaks of the Cr-doped Zinc cobaltite (Figure 4.1) are observed at 31.2°, 36.8°, 38.5°, 44.7°, 55.7°, 59.3°, 65.2°, 78.2° and their corresponding miller indices are (220), (311), (222), (400), (422), (511), (440), (622) which is shown in the (Table 4.1). The observed pattern nicely coincides with the stick patterns of JCPDS Card No.: 23-1390 indicating the formation of spinel-cubic symmetry having a structural formula AB_2O_4 with $Fd\bar{3}m$ space group. There are no extra peaks observed proving a good structural stability even after doping with chromium.

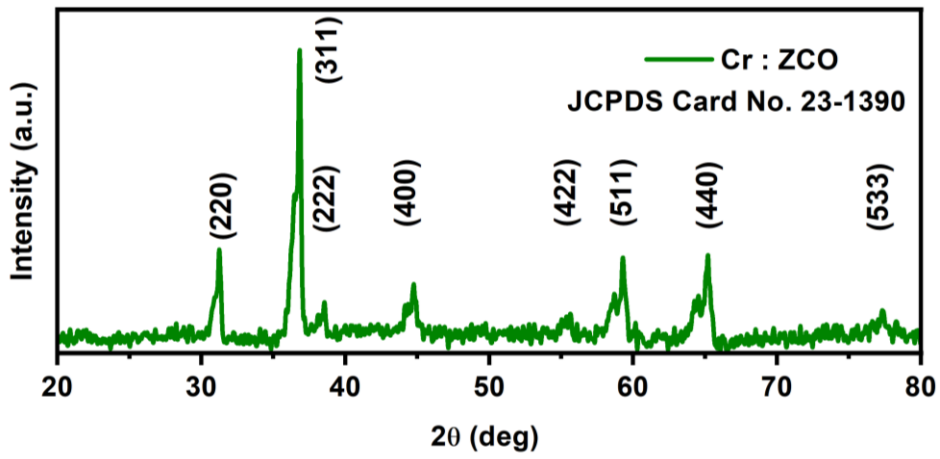

Fig 4.1 XRD pattern of Chromium doped with Zinc cobaltite

Table 4.1 Indexing planes for Chromium doped Zinc cobaltite

No. of peaks	2θ (deg)	h	k	l
1	31.24	2	2	0
2	36.83	3	1	1
3	38.50	2	2	2
4	44.74	4	0	0
5	55.35	4	2	2
6	59.28	5	1	1
7	65.14	4	4	0
8	78.32	5	3	3

The crystallite size of the as-prepared sample is calculated by using the Debye-Scherrer formula. The Debye Scherrer formula is

$$\mathbf{L} = \frac{k\lambda}{\beta \cos\theta}\ \mathbf{(nm)}$$

where,

k is Scherrer constant,

λ is the wavelength of the radiation (1.5406Å)

β is Full width half maximum of the peak.

The most prominent and highly intense peak at 36.803° corresponds to the plane (311) of Cr doped Zinc cobaltite. The crystallite size is 94.33 nm for Chromium doped Zinc Cobaltite calculated from (311) plane which is shown in Table (4.2, 4.3). The observed peaks are sharp and intense which indicates the high crystallinity of the sample.

Table 4.2 Crystallite size of the major diffraction peaks of Chromium doped in Zinc cobaltite

Sample	2θ	β – FWHM (deg)	Crystallite size (nm)
Cr: Zinc cobaltite	36.83	0.0888	94.88
	31.24	0.1319	62.56
	59.28	0.1562	58.53

Table 4.3 Crystallite size and lattice parameters of Chromium doped with Zinc cobaltite

Sample	Crystallite Size (nm)	a (Å) from JCPDS No. 23-1390	V $(Å)^3$ from JCPDS No. 23-1390
Cr: Zinc cobaltite	94.88	8.09	530.81

4.1.2 XRD Analysis of Lanthanum doped in Zinc cobaltite:

Other type of trivalent elements chosen for doping in Zinc cobaltite lattice are La^{3+} and Dy^{3+}. Lanthanum (La^{3+}) is the second most reactive among the rare-earth metals after europium with the oxidation state of 3+. Lanthanum is doped with Zinc cobaltite with 0.02 M concentration and is shown in Figure 4.2. The diffraction peaks of the La-doped Zinc cobaltite sample are observed at 25.03°, 30.4°, 33.6°, 36.8°, 38.5°, 40.3°, 43.8°, 44.7°,50.5°, 51.2°, 56.6°, 59.3°, 63.6°, 65.2°, 75.3°, 78.3° are marked with their corresponding miller indices (110), (220), (112), (311), (222), (020), (400), (220), (120), (121), (422), (511), (230), (440), (343), (533). The obtained pattern is well matched with the pure Zinc cobaltite JCPDS Card No. 23-1390 with a cubic structure, and some extra peaks 25.03°, 33.6°, 40.3°, 43.8°, 50.5°, 51.2°, 63.6°, 75.3° are observed while doping upon La^{3+} which is indexed to the JCPDS Card No. 84-0848 of $LaCoO_3$ compound of the structure rhombohedral with the lattice parameter value of a = 5.377 Å with the volume

245.84 $Å^3$ and it lies in the space group of $R\bar{3}c$. The secondary phase formation of $LaCoO_3$ is evident from the XRD analysis of the La-doped Zinc cobaltite sample.

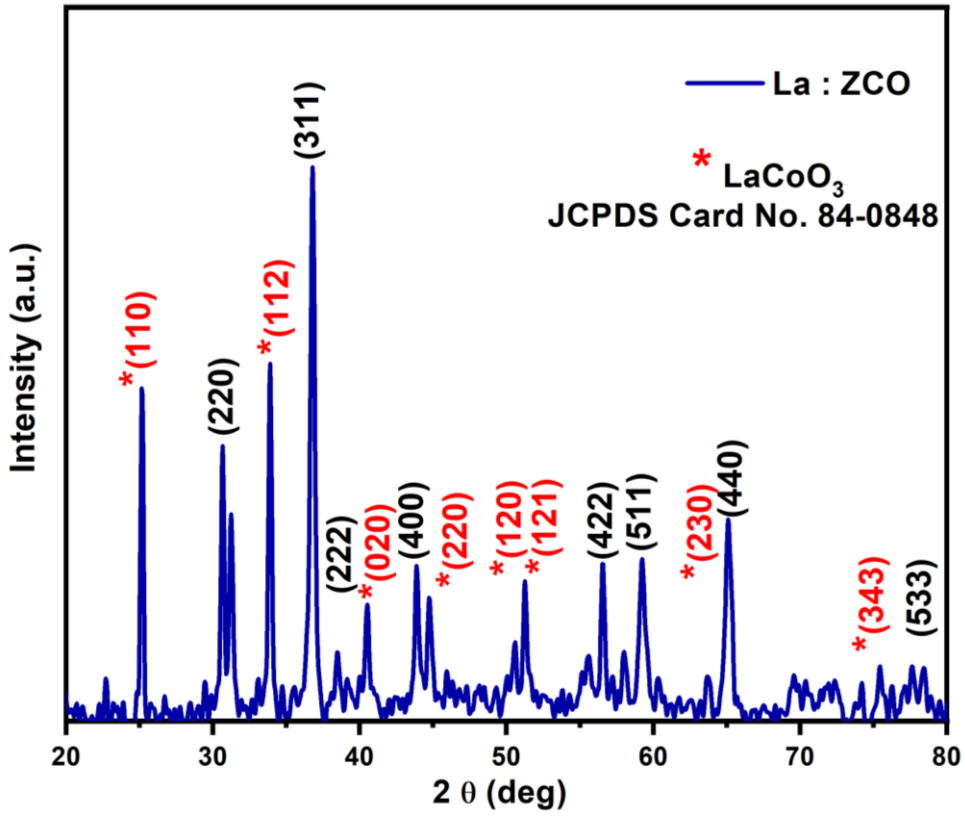

Fig 4.2 XRD pattern of Lanthanum doped with Zinc cobaltite

Table 4.4 Indexing planes for Lanthanum doped Zinc cobaltite

No. of peaks	2θ (deg)	h	k	l
1	25.03	1	1	1
2	31.43	2	2	0
3	33.65	1	1	2
4	36.83	3	1	1
5	38.36	2	2	2

6	40.31	0	2	0
7	44.74	4	0	0
8	50.50	1	2	0
9	51.22	1	2	1
10	55.35	4	2	2
11	59.25	5	1	1
12	63.62	2	3	0
13	65.14	4	4	0
14	75.30	3	4	3
15	78.30	5	3	3

The most prominent and highly intense peak at 36.83° corresponds to the plane (311) of La-doped Zinc cobaltite. The crystallite size is 37.74 nm for Lanthanum doped Zinc Cobaltite calculated from (311) plane. The observed peaks are sharp and intense.

Table 4.5 Crystallite size of the major diffraction peaks of Lanthanum doped in Zinc cobaltite

Sample	**2θ**	**β – FWHM (deg)**	**Crystallite size (nm)**
La: Zinc cobaltite	36.77	0.3107	37.74
	31.22	0.3107	26.56
	55.68	0.1775	22.89

4.1.3 Dysprosium doped in Zinc cobaltite:

Dysprosium is doped with Zinc cobaltite in the trivalent group of elements. Dysprosium is a relatively hard metal and is silvery-white in its pure form. It is doped with Zinc cobaltite with the same 0.02 M concentration. The diffraction peaks of the pristine sample at 25.04°, 31.1°,32.3°, 35.4°, 36.7°, 38.5°, 40.8°, 43.8°, 44.7°,46.6°, 52.9°, 55.5°, 59.3°, 65.2°, 77.1° are marked with their corresponding miller indices (211), (220), (222), (321), (311), (222), (411), (400), (332), (521), (422), (511), (440), (533). The obtained pattern matches with the JCPDS Card No.: 23-1390 of pure Zinc cobaltite has a cubic structure and some extra peaks 25.04°, 32.3°, 35.4°, 40.8°, 43.8°,46.6°, 52.9° are observed while doping upon Dy^{3+} which is indexed to the JCPDS Card No. 22-0612 of Dy_2O_3 compound of the structure cubic with the lattice parameter value of a =10.66 Å and it lies in the space group of $Ia\bar{3}$. This need not be considered as a secondary phase due to the fact that Dysprosium occupies the Cobalt site for Dy – O bonding which is a body centered cubic phase.

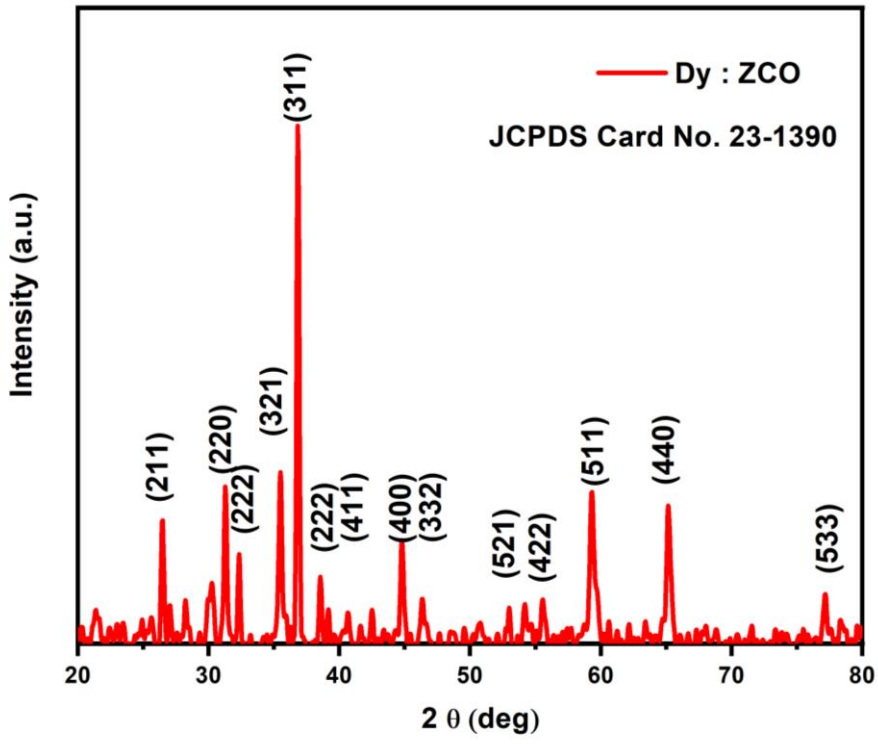

Fig 4.3 XRD pattern of Dysprosium doped with Zinc cobaltite

Table 4.6 Indexing planes for Dysprosium doped Zinc cobaltite

No. of peaks	2θ (deg)	h	k	l
1	25.04	2	1	1
2	31.13	2	2	0
3	32.39	2	2	2
4	35.48	3	2	1
5	36.74	3	1	1
6	38.58	2	2	2
7	40.80	4	1	1
8	44.74	4	0	0
9	46.63	3	3	2
10	52.90	5	2	1
11	55.53	4	2	2
12	59.36	5	1	1
13	65.20	4	4	0
14	77.17	5	3	3

The most prominent and highly intense peak at 36.74° corresponds to the plane (311) of Dy doped Zinc cobaltite. The crystallite size is 47.19 nm for Dysprosium doped Zinc cobaltite calculated from (311) plane.

Table 4.7 Crystallite size of the major diffraction peaks of Dysprosium doped in Zinc cobaltite

Sample	2θ	β – FWHM (deg)	Crystallite size (nm)
Dy: Zinc cobaltite	36.82	0.1775	47.19
	31.27	0.1775	46.49
	55.54	0.2100	43.54

Table 4.8 Comparison of crystallite size values of Zinc cobaltite samples

Sample	$2\theta_{(311)}$	β (FWHM) (311)	Crystallite size (311) (nm)
Cr: Zinc cobaltite	36.83	0.0888	94.88
La: Zinc cobaltite	36.77	0.3107	37.74
Dy: Zinc cobaltite	36.82	0.1775	47.19

A comparison of the three dopants, Chromium doped Zinc cobaltite are shown in Table 4.8. Chromium doped Zinc cobaltite exhibits the highest crystallite size with 94.88 nm

4.2 Cyclic Voltammetric (CV) Analysis:

Cyclic Voltammetry (CV) analysis for the Zinc cobaltite with dopants is performed by electrochemical workstation (Biologic SP150). The reversibility of a process, an analyte's diffusion coefficient, and its reduction potential can all be determined using cyclic voltammetry.

Figure 4.4 shows the CV profile of Chromium doped Zinc cobaltite with the electrolytic concentration of 1M-LiOH at different scan rates ranging from 20mV/s to 100mV/s.

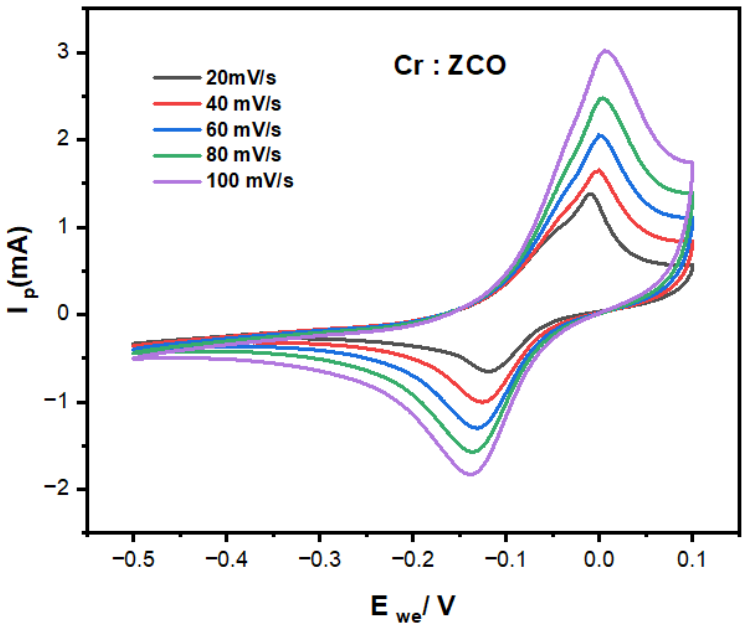

Figure 4.4 CV profile of Cr-doped Zinc cobaltite with 1M LiOH

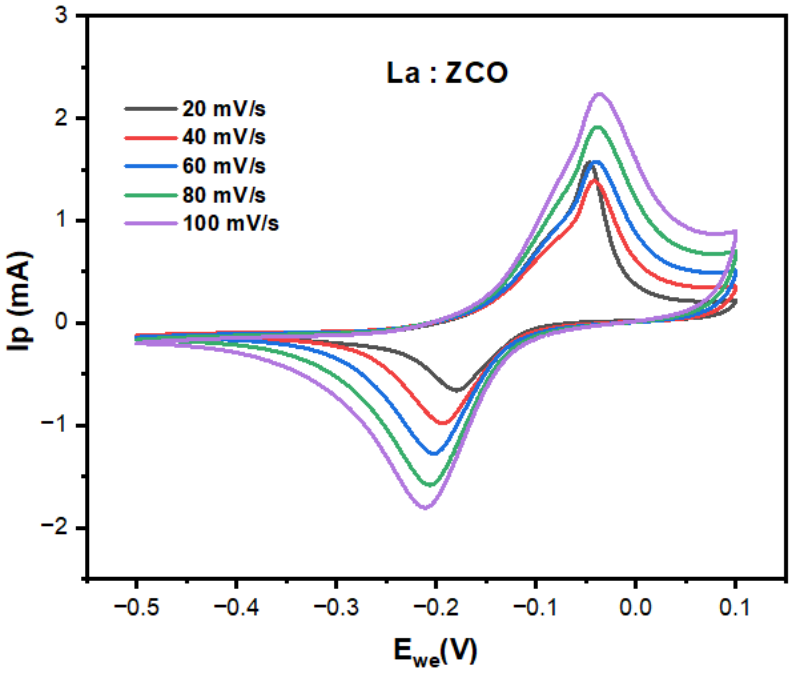

Figure 4.5 CV profile of La-doped Zinc cobaltite with 1M LiOH

Figure 4.5 shows that the CV profile of Lanthanum doped Zinc cobaltite with the electrolytic concentration of 1M-LiOH at different scan rates ranging from 20mV/s to 100mV/s.

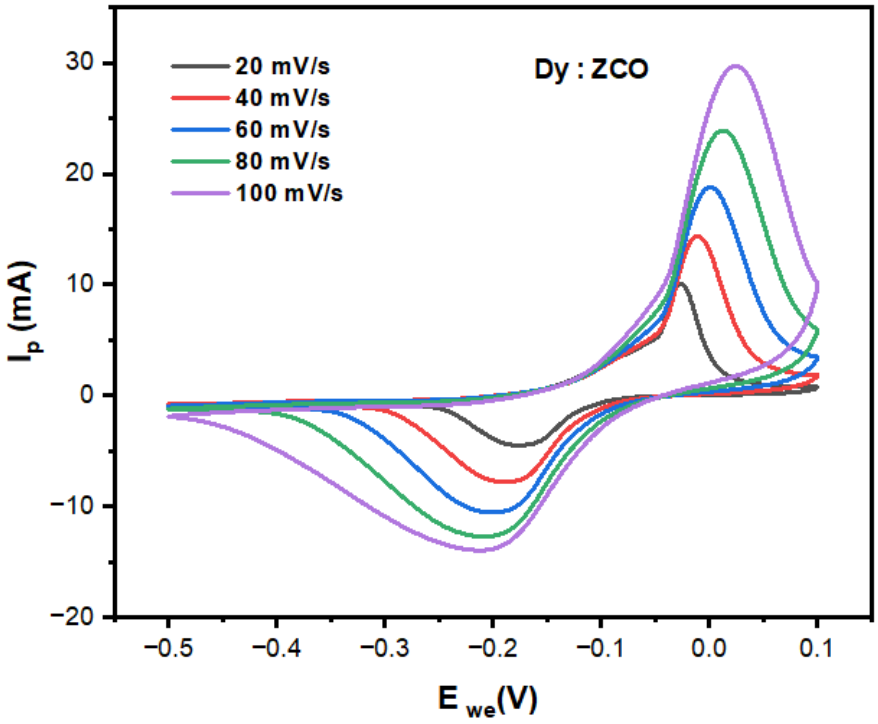

Figure 4.6 CV profile of Dy-doped Zinc cobaltite with 1M LiOH

Figure 4.6 shows that the CV profile of Dysprosium doped Zinc cobaltite with the electrolytic concentration of 1M-LiOH at different scan rates ranging from 20mV/s to 100mV/s.

The redox activity for all the samples is observed in the potential window ranging from -0.5V to +0.1V.

The oxidation and reduction peaks of Cr doped Zinc cobaltite in LiOH are 0.006V and -0.138V, in LiOH electrolyte. The oxidation and reduction peaks of La-doped Zinc cobaltite in LiOH are -0.037 V and -0.212 V. The oxidation and reduction peaks of Dy-doped Zinc cobaltite in LiOH are 0.023 V and -0.207 V.

The capacity retention and fading are determined by continuous number of cycling with a higher scan rate. Hence, the stability of the as-prepared sample in LiOH electrolytes are observed over 100 numbers of cycles at the scan rate of 100 mV/s. The Cr doped Zinc cobaltite and Dy doped Zinc cobaltite in 1M LiOH electrolytic solution shows a better stability than La doped Zinc cobaltite.

The prerequisites for a reversible electrochemical system (Nernstian system) are,

(i) Unity in peak current ratio,

(ii) Linearity between square root of scan rate and peak current,

(iii) Constant peak potential for different scan rates and

(iv) Peak separation more than or equal to 59 mV.

Figure 4.7 shows the linearity between square root of the scan rate vs peak current for Cr doped Zinc cobaltite. Figure 4.8 shows the linearity between scan rate and the peak potential for Cr doped Zinc cobaltite.

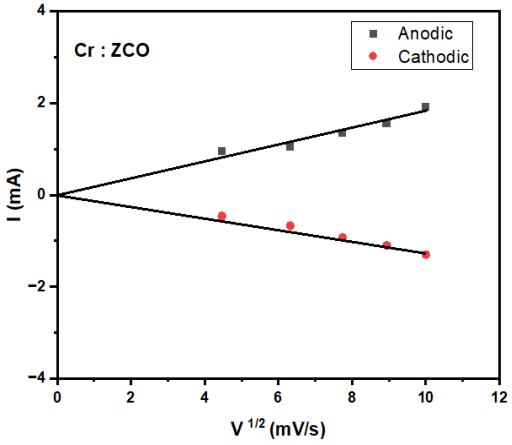

Fig 4.7 Plot of scan rate Vs peak current for Cr-doped in Zinc cobaltite

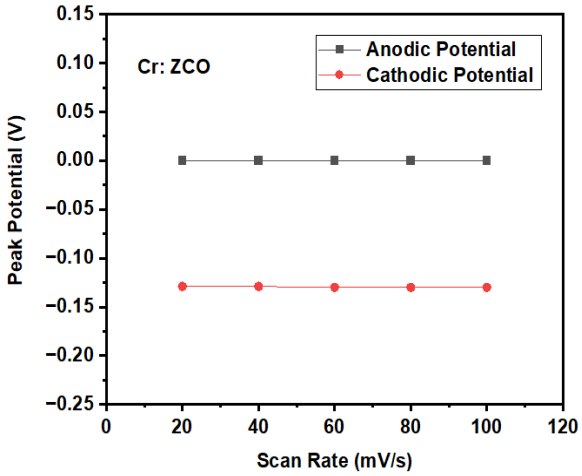

Fig 4.8 Plot between scan rate & peak for Cr-doped in Zinc cobaltite

The independency of peak current with scan rate and peak potential with scan rate is observed from the CV graphs of the as-prepared sample Cr doped Zinc cobaltite in 1M LiOH electrolytic solution for different scan rates are shown in Figure 4.7 and 4.8 respectively.

Figure 4.9 shows the linearity between square root of the scan rate vs peak current for La doped Zinc cobaltite. Figure 4.10 shows the linearity between scan rate and the peak potential for La doped Zinc cobaltite.

The independency of peak current with scan rate and peak potential with scan rate is observed from the CV graphs of the as-prepared sample La doped Zinc cobaltite in 1M

LiOH electrolytic solution for different scan rates are shown in Figure 4.9 and 4.10 respectively.

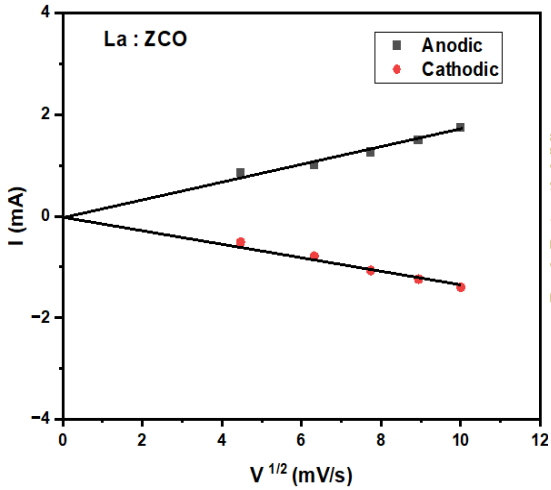

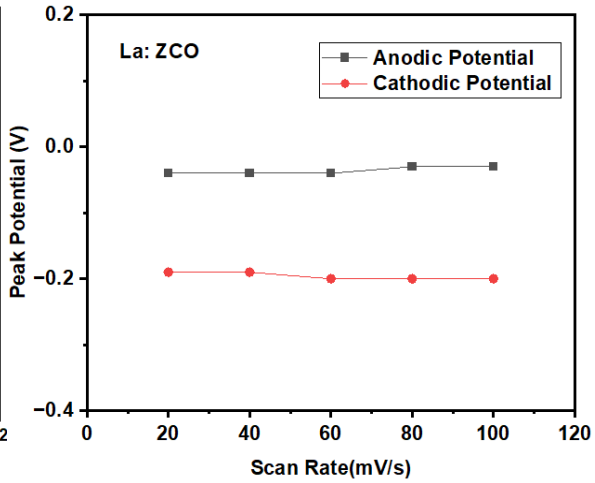

Fig 4.9 Plot of scan rate Vs peak current for La-doped in Zinc cobaltite

Fig 4.10 Plot between scan rate & peak potential for La-doped in Zinc cobaltite

Figure 4.11 shows the linearity between square root of the scan rate vs peak current for Dy doped Zinc cobaltite. Figure 4.12 shows the linearity between scan rate and the peak potential for Dy doped Zinc cobaltite.

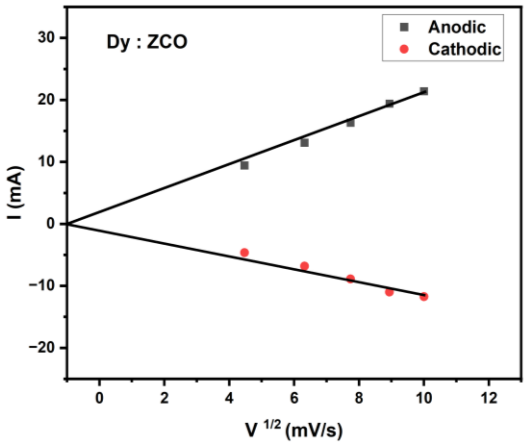

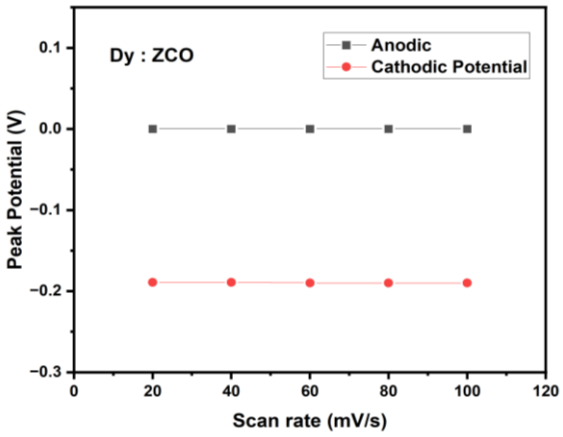

Fig 4.11 Plot of scan rate Vs peak current for Dy-doped Zinc cobaltite

Fig 4.12 Plot between scan rate & peak potential for Dy-doped Zinc cobaltite

The independency of peak current with scan rate and peak potential with scan rate is observed from the CV graphs of the as-prepared sample Dy doped Zinc cobaltite in 1M LiOH electrolytic solution for different scan rates are shown in Figure 4.11 and 4.12 respectively.

Among all the samples, the Chromium doped Zinc Cobaltite shows a different value of reduction potential when compared to Lanthanum and Dysprosium doped Zinc cobaltite. Generally, when scan rate increases, the charging current will increase. Peak current values of Dy doped with Zinc cobaltite in LiOH electrolyte are exorbitantly high and well defined.

Reviewing all the above performances, it is clearly seen that the Nernstian condition are well satisfied with all three doped samples, where Chromium doped with Zinc cobaltite (ZCO) shows a ratio of IP_c/IP_a nearly equal to 1 which shows the reversible nature of the sample. Also, Lanthanum and Dysprosium doped with Zinc cobaltite shows a slight deviation from the standard reversible nature, which can be described as a quasi reversible nature.

In all the three cases, with respect to the ratio of IP_c/ IP_a, reversibility of Chromium > Lanthanum > Dysprosium respectively. The peak potentials are well maintained constant during the CV profiling.

The diffusion coefficient of the electrochemical cells constructed using the sample with LiOH electrolyte are given in the Table 4.11, 4.12, 4.13 for Chromium doped Zinc cobaltite, Lanthanum doped Zinc cobaltite and Dysprosium doped Zinc cobaltite respectively.

The diffusion coefficient is calculated by using the formula,

$$\mathbf{D} = \left(\frac{\boldsymbol{B}}{\mathbf{2.69\times10^5}\ \boldsymbol{A\ Cn^{3/2}}}\right)^{\mathbf{2}}$$

Where,

B - Slope of the linear plot (mole/second)

A - Area of the electrode $(cm)^2$

C - Concentration of electrolyte (mole/ liter)

The value obtained from the linear plot of Cr doped Zinc cobaltite is shown in the Table 4.9.

Table 4.9 CV analysis of Chromium doped Zinc cobaltite with 1M-LiOH electrolyte

Scan rate (mV/s)	Potential (V)		Current (mA)		$\lvert E_{red}-E_{ox}\rvert$	$\lvert I_{cathodic}/I_{anodic}\rvert$	Diffusion Coefficient cm^2/s
	E_{ox}	E_{red}	I_{ox}	I_{red}			
20	-0.009	-0.129	0.95	-0.46	0.12	0.38	Anodic 4.5917×10^{-13}
40	-0.001	-0.129	1.04	-0.67	0.12	0.64	
60	0.002	-0.130	1.34	-0.93	0.12	0.69	
80	0.002	-0.130	1.56	-1.10	0.12	0.70	
100	0.006	-0.131	1.91	-1.30	0.12	0.68	Cathodic 2.027×10^{-13}

The value obtained from the linear plot of La doped Zinc cobaltite is shown in the Table 4.10.

Table 4.10 CV analysis of Lanthanum doped Zinc cobaltite with 1M-LiOH electrolyte

Scan rate (mV/s)	Potential (V)		Current (mA)		$\lvert E_{red}-E_{ox}\rvert$	$\lvert I_{cathodic}/I_{anodic}\rvert$	Diffusion Coefficient cm^2/s
	E_{ox}	E_{red}	I_{ox}	I_{red}			
20	-0.040	-0.190	0.85	-0.51	0.15	0.60	Anodic 3.9419×10^{-13}
40	-0.040	-0.190	1.01	-0.79	0.15	0.78	
60	-0.041	-0.204	1.26	-1.07	0.16	0.84	
80	-0.038	-0.205	1.49	-1.24	0.16	0.83	Cathodic 2.5403×10^{-13}
100	-0.039	-0.206	1.74	-1.40	0.16	0.80	

The value obtained from the linear plot of Dysprosium doped Zinc cobaltite is shown in Table 4.11.

Table 4.11 CV analysis of Dysprosium doped Zinc cobaltite with 1M-LiOH electrolyte

Scan rate (mV/s)	Potential (V)		Current (mA)		$\lvert E_{red}-E_{ox}\rvert$	$\lvert I_{cathodic}/I_{anodic}\rvert$	Diffusion Coefficient cm^2/s
	E_{ox}	E_{red}	I_{ox}	I_{red}			
20	-0.001	-0.189	9.42	-4.65	0.18	0.49	Anodic
40	-0.001	-0.189	13.10	-6.83	0.18	0.52	6.2733×10^{-11}
60	0.002	-0.190	16.32	-8.89	0.18	0.54	
80	0.002	-0.190	19.40	-11.00	0.18	0.56	Cathodic
100	0.002	-0.191	21.40	-11.76	0.18	0.54	1.8461×10^{-11}

In the case of Dysprosium doped with Zinc cobaltite, the anodic potential shift towards the positive window upon increasing the scan rate to 100 mV/s, showing a quasi-reversible behavior of the sample.

The term “specific capacity” is used to describe an electrode's performance. Specific capacity defines the amount of electric charge (“milliampere hours” or mAh) the material can deliver per gram of a material. In a lithium-ion battery, the carrier of the electric charge is the positively-charged lithium ion.

The specific capacity is calculated by using the formula,

$$C = \int \frac{I\,dv}{vmV} \quad F\,g^{-1}$$

where,

$\int I\,dv$ – Integral area of the curve (A.V),

v – Scan rate (mV/s),

m - mass of the active material (g),

V - potential window (V).

Table 4.12 Specific capacity of the samples doped in Zinc cobaltite

Sample	Mass loading (g)	Specific capacity (mAh/g)
Dy: Zinc cobaltite	0.0023	53.15
Cr: Zinc cobaltite	0.0027	14.36
La: Zinc cobaltite	0.0030	3.38

The specific capacity of all three dopants Chromium doped Zinc cobaltite, Lanthanum doped Zinc cobaltite, Dysprosium doped Zinc cobaltite for the scan rate of 10 mV/s are compared in the Table 4.12.

From this Table 4.12, it is evident that the highest specific capacity of 53.15 mAh/g is observed for Dysprosium doped Zinc cobaltite for the scan rate of 10 mV/s. Because of the minimal mass loading in Dysprosium doped Zinc cobaltite, the specific capacity and the diffusion coefficient has been increased. Dysprosium as an element exhibits good electronic conductivity compared to the other dopants chosen hence showing good electrochemical activity. The fact that Dysprosium occupied the Cobalt site contrarily Lanthanum and Chromium occupied the Zinc site breaks a big difference in the electrochemical performance. It is evident that preserving cubic lattice with substitution of larger ionic radii element instead of Cobalt with the same oxidation state is the most favorable condition for improvement in electrochemical behavior.

CHAPTER V

SUMMARY AND CONCLUSION

Zinc cobaltite is doped with three trivalent elements by Sol-gel method. The prepared sample is analysed for structural determination using XRD which confirmed the cubic structure. The three samples show a high intense peak at 36.803° which corresponds to the plane (311). The crystallite size of the three samples are calculated. The crystallite size of Chromium doped Zinc cobaltite is 94.8883 nm. Lanthanum and Dysprosium has relatively lower crystallite size which are 37.74 nm and 47.19 nm respectively. The three samples are tested for cyclability with 1M LiOH as electrolyte, Zinc cobaltite doped with Chromium, Lanthanum and Dysprosium as the working electrode, Pt is employed as a counter electrode and Ag/AgCl is used as reference electrode. The cyclability is tested over 100 cycles for the three samples. The Chromium doped Zinc cobaltite and Dysprosium doped Zinc cobaltite in 1M LiOH electrolytic solution shows a better stability than Lanthanum doped Zinc cobaltite. Chromium doped Zinc cobaltite shows a different value of reduction potential when compared to Lanthanum and Dysprosium doped Zinc cobaltite. Generally, when scan rate increases, the charging current will increase. Peak current values of Dysprosium doped Zinc cobaltite in LiOH electrolyte are exorbitantly high and well defined. The peak potentials are well maintained in all three samples. The Nernstian condition is satisfied by all the three samples. The mass loading is minimal for Dysprosium, so the specific capacity is comparatively high 53.15 mAh/g than other samples Chromium and Lanthanum. Also, the Diffusion coefficient is higher for Dysprosium doped Zinc cobaltite (D_{anodic} = 6.2733 $\times 10^{-11}$ cm^2/s, $D_{cathodic}$ = 1.8461 $\times 10^{-11}$ cm^2/s), when compared with Lanthanum and Chromium doped Zinc cobaltite. Dysprosium occupied the Cobalt site, contrarily Lanthanum and Chromium occupied the Zinc site, which breaks a big difference in the electrochemical performance. It is observed that the preserving cubic lattice with substitution of larger ionic radii element instead of Cobalt with the same oxidation state is the most favorable condition for improvement in electrochemical behavior. Hence proving Dysprosium doped Zinc cobaltite could be used as a cathode for Lithium-ion batteries.

REFERENCES

[1] Edy Riyanto, Tony Kristiantoro, Erie Martides, Dedi, Budi Prawara, Dadang Mulyadi, Suprapto, Lithium-ion battery performance improvement using two-dimensional materials, Materials today, 2023, DOI: https://doi.org/10.1016/j.matpr.2023.02.392.

[2] Felix Katzer, Michael A. Danzer, Analysis and detection of lithium deposition after fast charging of lithium-ion batteries by investigating the impedance relaxation, Journal of Power Sources, 503, 230009, 2021, DOI: 10.1016/j.jpowsour.2021.230009.

[3] Changlong Li, Naxin Cui, Zhongrui Cui, Chunyu Wang, Chenghui Zhang, Novel equivalent circuit model for high-energy lithium-ion batteries considering the effect of nonlinear solid-phase diffusion, Journal of Power Sources, 523, 230993, 2022, DOI: 10.1016/j.jpowsour.2022.230993.

[4] Farschad Torabi, Pouria Ahmadi, Chapter 2 - Fundamentals of batteries, Simulation of Battery Systems, Fundamentals and Applications, 55-81, 2020, DOI: 10.1016/B978-0-12-816212-5.00006-4.

[5] John T. Warner, Chapter 2 - Electrochemistry basics, Lithium-Ion Battery Chemistries, 17-41, 2019, DOI: 10.1016/B978-0-12-814778-8.00002-8.

[6] Xiaohui Li, Shuaiwei Liu, Jiachao Yang, Zhenjiang He, Junchao Zheng, Yunjiao Li, Electrochemical methods contribute to the recycling and regeneration path of lithium-ion batteries, Energy Storage Materials, 55, 606-630, 2022, DOI: 10.1016/j.ensm.2022.12.022.

[7] Oscar E. Rojas, Muhammad A. Khan, A review on electrical and mechanical performance parameters in lithium-ion battery packs, Journal of Cleaner Production, 378, 2022, DOI: 10.1016/j.jclepro.2022.134381.

[8] Minghai Shen, Hailing M, Metal-organic frameworks (MOFs) and their derivative as electrode materials for lithium-ion batteries, Coordination Chemistry Reviews, 470, 2022, DOI: 10.1016/j.ccr.2022.214715.

[9] Asad Ali, Fengxing Liang, Jinliang Zhu, Pei Kang Shen, The role of graphene in rechargeable lithium batteries: Synthesis, functionalisation, and perspectives, Nano Materials Science, 2022, DOI: 10.1016/j.nanoms.2022.07.004.

[10] Gabriele Bandini, Gianluca Caposciutti, Mirko Marracci, Alice Buffi, Bernardo Tellini, Characterization of lithium-batteries for high power applications, Journal of Energy Storage, 50, June 2022, 104607, DOI: 10.1016/j.est.2022.104607.

[11] Foad H. Gandoman, Joris Jaguemont, Shovon Goutam, Rahul Gopalakrishnan, Yousef Firouz, Theodoros Kalogiannis, Noshin Omar, Joeri Van Mierlo, Concept of reliability and safety assessment of lithium-ion batteries in electric vehicles: Basics, progress, and challenges, Applied Energy, 251,113343, 2019, DOI: 10.1016/j.apenergy.2019.113343.

[12] Daniel Neb, Stanislav Kim, Henning Clever, Benjamin Dorn, Achim Kampker, Current advances on laser drying of electrodes for lithium-ion battery cells, Procedia CIRP, 107, 1577-1587, 2022, DOI: 10.1016/j.procir.2022.05.194.

[13] Nikolaos Wassiliadis, Manuel Ank, Leo Wildfeuer, Michael K. Kick, Markus Lienkamp, Experimental investigation of the influence of electrical contact resistance on lithium-ion battery testing for fast-charge applications, Applied Energy 295, 117064, 2021, DOI: 10.1016/j.apenergy.2021.117064.

[14] Damian Burzyński, Leszek Kasprzyk, A novel method for the modeling of the state of health of lithium-ion cells using machine learning for practical applications, Knowledge-Based Systems, 219, 106900, 2021, DOI: 10.1016/j.knosys.2021.106900.

[15] Isidor Buchmann, Batteries in a Portable World - A Handbook on Rechargeable Batteries for Non-Engineers, Battery university, ISBN 978-0968211847, 2016.

[16] Elham Samiei, Saeed Mohammadi, Masoud Torkzadeh-Mahani, Mohammad Bagher Askari, Preparation and Characterization of $ZnCo_2O_4$ as a Binary Transitional Metal Oxide Towards Pseudocapacitor Electrode Materials, Brazilian Journal of Physics 2021, 51:420–428, DOI: 10.1007/s13538-020-00845-9.

[17] G.G. Soundarya, B. Nalini, D. Lakshmi, P. Priyanka, Structural rearrangement by Ni, Cr doping in zinc cobaltite and its influence on supercapacitance, Ceramics International, 47, 18635–18645, 2021, DOI: 10.1016/j.ceramint.2021.03.195.

[18] A. Juliet Christina Mary, C.I. Sathish, PaskalisSahaya Murphin Kumar, Ajayan Vinu, A. Chandra Bose, Fabrication of hybrid supercapacitor device based on $NiCo_2O_4$@$ZnCo_2O_4$ and the biomass-derived N-doped activated carbon with a honeycomb structure, Electrochimica Acta, 2020, DOI: 10.1016/j.electacta.2020.136062.

[19] Gutturu Rajasekhara Reddy, Nadavala Siva Kumar, Borelli Deva Prasad Raju, Gnanendra Shanmugam, Ebrahim H. Al-Ghurabi and Mohammad Asif, Enhanced Supercapacitive Performance of Higher-Ordered 3D-Hierarchical Structures of Hydrothermally Obtained $ZnCo_2O_4$ for Energy Storage Devices, Nanomaterials, 10, 1206, 2020, DOI: 10.3390/nano10061206.

[20] M. Priya, V.K. Premkumar, P. Vasantharani, G. Sivakumar, Structural and electrochemical properties of $ZnCo_2O_4$ nanoparticles synthesized by hydrothermal method, Vacuum, 2019, DOI: 10.1016/j.vacuum.2019.06.020.

[21] Meenu Sharma, and Anurag Gaur, Cu Doped Zinc Cobalt Oxides Based Solid State Symmetric Supercapacitors: A Promising Key for High Energy Density, The Journal of Physical Chemistry, 2019, DOI: 10.1021/acs.jpcc.9b08170.

[22] Loubna Merabet, Kamel Rida, Nawel Boukmouche, Sol-gel Synthesis, Characterization, and Supercapacitor Applications of MCo_2O_4 (M = Ni, Mn, Cu, Zn) Cobaltite Spinels, Ceramics International, 2018, DOI: 10.1016/j.ceramint.2018.03.171.

[23] A. Juliet Christina Mary, S. Thilagavathi, and A. Chandra Bose, Influence of different synthesis approach on $ZnCo_2O_4$ nanomaterial and its supercapacitor behavior, American Institute of Physics, 2018, DOI: 10.1063/1.5029173.

[24] Zhiyong Gao, Lingcui Zhang, Jiuli Chang, Zhen Wang, Dapeng Wu, Fang Xu, Yuming Guo, Kai Jiang, $ZnCo_2O_4$-reduced graphene oxide composite with balanced capacitive performance in asymmetric supercapacitors, Applied Surface Science 442 138–147, 2018, DOI: 10.1016/j.apsusc.2018.02.152.

[25] B. Saravanakumar, G. Ravi, R. Yuvakkumar, V. Ganesh, S. Ravichandran, M. Thambidurai, A. Sakunthala, Hydrothermal synthesis and electrochemical properties of $ZnCo_2O_4$ microspheres, Springer, 2018, DOI: 10.1007/s11581-018-2766-1.

[26] Vijay Kumar, and C. R. Mariappan, Electrochemical performance of spinel-type Ni doped $ZnCo_2O_4$ mesoporous rods as an electrode for supercapacitors, American Institute of Physics, 2018, DOI: 10.1063/1.5035232.

[27] Huiyu Chen, Jinpeng Wang, Xingrong Han, Fan Liao, Yanfei Zhang, Xinghua Han, Chunju Xu, Simple growth of mesoporous zinc cobaltite urchinlike microstructures towards high-performance electrochemical capacitors, Ceramics International, 2018, DOI: 10.1016/j.ceramint.2018.11.172.

[28] John Anthuvan Rajesh, Bong-Ki Min, Jae-Hong Kim, Soon-Hyung Kang, Hyunsoo Kim, Kwang-Soon Ahn, Facile hydrothermal synthesis and electrochemical supercapacitor performance of hierarchical coral-like $ZnCo_2O_4$ nanowires, Journal of Electroanalytical Chemistry 785, 48–57, 2017, DOI: 10.1016/j.jelechem.2016.12.027.

[29] Xuechun Xiao, Guofeng Wang, Mengmeng Zhang, Zhezhe Wang, Rongjun Zhao, Yude Wang, Electrochemical performance of mesoporous $ZnCo_2O_4$ nanosheets as an electrode material for supercapacitor, Springer, 2017, DOI: 10.1007/s11581-017-2354-9.

[30] Qichong Zhang, Weiwei Xu, Juan Sun, Zhenghui Pan, Jingxin Zhao, Xiaona Wang, Jun Zhang, Ping Man, Jiabin Guo, Zhenyu Zhou,Bing He, Zengxing Zhang, Qingwen Lia, Yuegang Zhang, Lai Xu and Yagang Yao, Constructing Ultrahigh-Capacity Zinc-Nickel-Cobalt Oxide@$Ni(OH)_2$ Core-Shell Nanowire Arrays for High-Performance Coaxial Fiber-Shaped Asymmetric Supercapacitors, ACS Publications, 2017, DOI: 10.1021/acs.nanolett.7b03507.

[31] A Juliet Christina Mary and A Chandra Bose, Hydrothermal synthesis of Mn-doped $ZnCo_2O_4$ electrode material for high performance Supercapacitor, APSUSC, 2017, DOI: 10.1016/j.apsusc.2017.06.313.

[32] Chun Wu, Junjie Cai, Qiaobao Zhang, Xiang Zhou, Ying Zhu, Peikang Shen, and Kaili Zhang, Hierarchical Mesoporous Zinc-Nickel-Cobalt Ternary Oxide Nanowire Arrays on Nickel Foam as High Performance Electrodes for Supercapacitors, ACS Applied Materials & Interfaces, 2015, DOI: 10.1021/acsami.5b07607.

[33] Wenlong Bai, Hao Tong, Zhenzhen Gao, Shihong Yue, Sichuan Xing, Shengyang Dong, Laifa Shen, Jianping He, Xiaogang Zhang, Yanyu Liang, Preparation of $ZnCo_2O_4$ Nanoflowers on 3D Carbon Nanotube/Nitrogen-Doped Graphene Film and its Electrochemical Capacitance, Journal of Materials Chemistry A, 2015, DOI: 10.1039/C5TA05798A.

[34] Jinbing Cheng, Yang Lu, Kangwen Qiu, Hailong Yan, Xiaoyi Hou, Jinyou Xu, Lei Han, Xianming Liu, Jang-Kyo Kim and Yongsong Luo, Mesoporous $ZnCo_2O_4$ nanoflakes grown on nickel foam as electrodes for high performance supercapacitors, Physical Chemistry Chemical Physics, 2015, DOI: 10.1039/C5CP01629K.

[35] Gang Zhou, Jian Zhu, Yuejiao Chen, Lin Mei, Xiaochuan Duan, Guanhua Zhang,Libao Chen, Taihong Wang, Bingan Lu, Simple method for the preparation of highly porous $ZnCo_2O_4$ nanotubes with enhanced electrochemical property for supercapacitor, Electrochimica Acta 123, 450–455, 2014, DOI: 10.1016/j.electacta.2014.01.018.

[36] Marauo Davis, Cenk Gu¨meci, Bria Black, Carol Korzeniewski and Louisa Hope-Weeks, tailoring cobalt doped zinc oxide nanocrystals with high capacitance activity: factors affecting structure and surface morphology, RSC Advances, 2061–2066, 2011, DOI: 10.1039/c2ra00793b.

[37] Shubo Wang, Jun Pu, Yao Tong, Yuanyuan Cheng, Yan Gao and Zhenghua Wang, $ZnCo_2O_4$ nanowire arrays grown on nickel foam for high-performance pseudocapacitors, Journal of Materials Chemistry A, 2014, DOI: 10.1039/c3ta14941b.

[38] Bingkun Guan, Di Guo, Lingling Hu, Guanhua Zhang, Tao Fu, Weiji Ren, Jidong Li and Qiuhong Li, Facile synthesis of $ZnCo_2O_4$ nanowire cluster arrays on Ni foam for high-performance asymmetric supercapacitors, Journal of Materials Chemistry A, 2, 16116–16123, 2014, DOI: 10.1039/c4ta02378a.

[39] Hao Wu, Zheng Lou, Hong Yang and Guozhen Shen, A flexible spiral-type supercapacitor based on $ZnCo_2O_4$ nanorod electrodes, The Royal Society of Chemistry, 2014, DOI: 10.1039/c4nr06336h.

[40] Bin Liu, Boyang Liu, Qiufan Wang, Xianfu Wang, Qingyi Xiang, Di Chen, and Guozhen Shen, New Energy Storage Option: Toward $ZnCo_2O_4$ Nanorods/Nickel Foam

Architectures for High-Performance Supercapacitors, ACS Applied Materials & Interfaces, 2013, DOI: 10.1021/am402339d.

[41] Subashchandrabose Thoka, Chih-Jung Chen, Anirudha Jena, Fu Ming Wang, Xing-Chun Wang, Ho Chang, Shu-Fen Hu, and Ru-Shi Liu, Spinel Zinc Cobalt Oxide (ZnCo2O4) Porous Nanorods as a Cathode Material for Highly Durable Li–CO_2 Batteries, ACS Applied Materials & Interfaces, 2020, DOI: 10.1021/acsami.9b21347.

[42] Lun Lu, Yan-Li Gao, Zhi-Zheng Yang, Cheng Wang, Jin-Guo Wang, Hui-Yuan Wang, Qi-Chuan Jiang, Template-free synthesis of mesoporous nanoring-like Zn-Co mixed oxides with high lithium storage performance, Journal of Power Sources 384, 256–263, 2018, DOI: 10.1016/j.jpowsour.2018.03.005.

[43] Mi-Hee Jung, The Two-Dimensional to Three-Dimensional Transition Structures of $ZnCo_2O_4$ for the Application of Lithium-Ion Batteries, APSUSC, 2017, DOI: 10.1016/j.apsusc.2017.08.055.

[44] Xiaoyi Hou, Shuai Bai, Song Xue, Xiaonan Shang, Yujun Fu, Deyan He, Wrinkled-paper-like $ZnCo_2O_4$ nanoflakes as a superior anode material for ultrahigh rate lithium-ion batteries, Journal of Alloys and Compounds, 2017, DOI: 10.1016/j.jallcom.2017.04.062.

[45] A. Yadav, Mashkoor A. Dar, P. Choudhary, P. Shah, and Dinesh Varshney, Chromium doping effects on structural and dielectric properties of Mn-Zn cobaltites, AIP Conference Proceedings 1728, 020301, 2016, DOI: 10.1063/1.4946352.

[46] Qiang Wang, Binwei Yu, Xiao Li, Lili Xing and Xinyu Xue, Core-shell Co_3O_4/$ZnCo_2O_4$ coconut-like hollow spheres with extremely high performance as anode materials for lithium-ion batteries, Journal of Materials Chemistry A, 2015, DOI: 10.1039/C5TA06872J.

[47] Guoxin Gao, Hao Bin Wu, Bitao Dong, Shujiang Ding, and Xiong Wen (David) Lou, Growth of Ultrathin $ZnCo_2O_4$ Nanosheets on Reduced Graphene Oxide with Enhanced Lithium Storage Properties, Advanced Science, 2015, 1400014, DOI: 10.1002/advs.201400014.

[48] Alok Kumar Rai, Trang Vu Thi, Baboo Joseph Paul, Jaekook Kim, Synthesis of nano-sized $ZnCo_2O_4$ anchored with graphene nanosheets as an anode material for secondary

lithium ion batteries, Electrochimica Acta 146, 577–584, 2014, DOI: 10.1016/j.electacta.2014.09.079.

[49] Haowen Liu, Jin Wang, One-pot synthesis of $ZnCo_2O_4$ nanorod anodes for high power Lithium ions batteries, Electrochimica Acta 92, 371– 375, 2013, DOI: 10.1016/j.electacta.2012.12.115.

[50] Lingling Hu, Baihua Qu, Chengchao Li, Yuejiao Chen, Lin Mei, Danni Lei, Libao Chen, Qiuhong Li, Taihong Wang, Facile synthesis of uniform mesoporous $ZnCo_2O_4$ microspheres as a high-performance anode material for Li-ion batteries, Journal of Materials Chemistry A, 5596–5602, 2013, DOI: 10.1039/c3ta00085k.

[51] Bin Liu, Jun Zhang, Xianfu Wang, Gui Chen, Di Chen, Chongwu Zhou, Guozhen Shen, Hierarchical Three-Dimensional $ZnCo_2O_4$ Nanowire Arrays/Carbon Cloth Anodes for a Novel Class of High-Performance Flexible Lithium-Ion Batteries, American Chemical Society, 3005−3011, 2012, DOI: 10.1021/nl300794f.

[52] Wei Luo, Xianluo Hu, Yongming Sun and Yunhui Huang, Electrospun porous $ZnCo_2O_4$ nanotubes as a high-performance anode material for lithium-ion batteries, Journal of Materials Chemistry, 8916–8921, 2012, DOI: 10.1039/c2jm00094f.

[53] Yongcai Qiu, Shihe Yang, Hong Deng, Limin Jinb and Weishan Li, A novel nanostructured spinel $ZnCo_2O_4$ electrode material: morphology conserved transformation from a hexagonal shaped nanodisk precursor and application in lithium ion batteries, Journal of Materials Chemistry, 20, 4439–4444, 2010, DOI: 10.1039/c0jm00101e.

[54] Xiuhua Wei, Donghua Chen∗, Wanjun Tang, Preparation and characterization of the spinel oxide $ZnCo_2O_4$ obtained by sol–gel method, Materials Chemistry and Physics 103, 54–58, 2007, DOI: 10.1016/j.matchemphys.2007.01.006.

[55] Changchun ai, Mingcai yin, Chiwei wang, Jutang Sun, Synthesis and characterization of spinel type $ZnCo_2O_4$ as a novel anode material for lithium ion batteries, Journal of Material Science 39 (2004) 1077 – 1079, 2003, DOI: 10.1023/B: JMSC.0000012948.27433.83.

[56] Yogesh Sharma, N. Sharma, G. V. Subba Rao, and B. V. R. Chowdari, Nanophase $ZnCo_2O_4$ as a High-Performance Anode Material for Li-Ion Batteries, Adv. Funct. Mater, 17, 2855–2861, 2007, DOI: 10.1002/adfm.200600997.

[57] M. V. Reddy, K. Y. H. Kenrick, Tang Ying Wei, Goh Yeow Chong, Goh Hock Leong, and B. V. R. Chowdari, Nano-$ZnCo_2O_4$ Material Preparation by Molten Salt Method and Its Electrochemical Properties for Lithium Batteries, Journal of The Electrochemical Society, 158 (12) A1423-A1430, 2011, DOI: 10.1149/2.089112jes.

[58] Ning Du, Yanfang Xu, Hui Zhang, Jingxue Yu, Chuanxin Zhai, and Deren Yang, Porous $ZnCo_2O_4$ Nanowires Synthesis via Sacrificial Templates: High-Performance Anode Materials of Li-Ion Batteries, American Chemical Society - Inorg. Chem., 50, 3320–3324, 2011, DOI: 10.1021/ic102129w.

[59] Beihong Liu, Hui Liu, Mengfang Liang, Lixiang Liu, Zhaolin Lv, Hang Zhou and Hong Guo, Controlled synthesis of hollow octahedral $ZnCo_2O_4$ nanocages assembled by untrathin 2D nanosheets for enhanced lithium storage, The Royal Society of Chemistry,2012, DOI: 10.1039/C7NR06259A.

[60] Zhipeng Sun, Wei Ai, Jilei Liu, Xiaoying Qi, Yanlong Wang, Jianhui Zhu, Hua Zhang and Ting Yu, Facile fabrication of hierarchical $ZnCo_2O_4$/NiO core/shell nanowire arrays with improved lithium-ion battery performance, The Royal Society of Chemistry, Nanoscale, 6, 6563–6568, 2014, DOI: 10.1039/c4nr00533c.

[61] Peng Yuan, Ning Zhang, Dan Zhang, Tao Liu, Limiao Chen,c Xiaohe Liu, Renzhi Ma and Guanzhou Qiu, Fabrication of nickel-foam-supported layered zinc–cobalt hydroxide nanoflakes for high electrochemical performance in supercapacitors, Chem. Commun., 11188—11191, 2014, DOI: 10.1039/c4cc05057f.

[62] Satyajit Ratha, Ruchita T. Khare, Mahendra A. More, Ranjit Thapa, Dattatray J. Late and Chandra Sekhar Rout, Field emission properties of spinel $ZnCo_2O_4$ microflowers, RSC Adv. 5372, 2014, DOI: 10.1039/c4ra10246k.

[63] Arnab Kanti Giri, Provas Pal, Ramadoss Ananthakumar, Muthirulandi Jayachandran, Sourindra Mahanty, and Asit Baran Panda, 3D Hierarchically Assembled Porous Wrinkled-Paper-like Structure of $ZnCo_2O_4$ and Co-ZnO@C as Anode Materials for Lithium-Ion Batteries, American Chemical Society, 2014, DOI: 10.1021/cg500282n.

[64] Jing Bai, Xiaogang Li, Guangzeng Liu, Yitai Qian, and Shenglin Xiong, Unusual Formation of $ZnCo_2O_4$ 3D Hierarchical Twin Microspheres as a High-Rate and Ultralong-Life Lithium-Ion Battery Anode Material, Adv. Funct. Mater., 24, 3012–3020, 2014, DOI: 10.1002/adfm.201303442.

[65] Youqi Zhu, Chuanbao Cao, Junting Zhang and Xingyan Xu, Two-dimensional ultrathin $ZnCo_2O_4$ nanosheets: general formation and lithium storage application, Journal of Materials Chemistry A, 2015, DOI: 10.1039/c5ta00808e.

[66] Hao Niu, Xue Yang, He Jiang, Dan Zhou, Xin Li, Ting Zhang, Jiuyu Liu, Qian Wang, Fengyu Qu, Hierarchical core-shell heterostructure of porous carbon nanofiber@$ZnCo_2O_4$ nanoneedle arrays: Advanced binder-free electrodes for all-solid-state supercapacitors, Journal of Materials Chemistry A, 2015, DOI: 10.1039/C5TA07439H.

[67] Xiaoli Ge, Zhaoqiang Li, Chengxiang Wang, and Long-wei Yin, Metal Organic Frameworks Derived Porous Core/Shell Structured ZnO/ $ZnCo_2O_4$/C Hybrids as Anodes for High-Performance Lithium-Ion Battery, ACS Applied Materials & Interfaces, 2015, DOI: 10.1021/acsami.5b08195.

[68] Bin Liu, Wu Xu, Pengfei Yan, Priyanka Bhattacharya, Ruiguo Cao, Mark E. Bowden, Mark H. Engelhard, Chong-Min Wang, and Ji-Guang Zhang, In Situ-Grown $ZnCo_2O_4$ on Single-Walled Carbon Nanotubes as Air Electrode Materials for Rechargeable Lithium–Oxygen Batteries, Chem Sus Chem, 8, 3697 – 3703, 2015, DOI: 10.1002/cssc.201500636.

[69] Yue Pan, Weijia Zeng, Lin Li, Yuzi Zhang, Yingnan Dong, Dianxue Cao, Guiling Wang, Brett L. Lucht, Ke Ye, Kui Cheng, A Facile Synthesis of $ZnCo_2O_4$ Nanocluster Particles and the Performance as Anode Materials for Lithium Ion Batteries, Nano-Micro Lett., 2016, DOI: 10.1007/s40820-016-0122-4.

[70] Qiaobao Zhang, Huixin Chen, Xiang Han, Junjie Cai, Yong Yang, Meilin Liu and Kaili Zhang, Graphene-Encapsulated Nanosheet-Assembled Zinc–Nickel–Cobalt Oxide Microspheres for Enhanced Lithium Storage, ChemSusChem, 186 – 196, 2016, DOI : 10.1002/cssc.201501151.

[71] Gracita M. Tomboc, Harsharaj S. Jadhav, Hern Kim, PVP assisted morphology-controlled synthesis of hierarchical mesoporous $ZnCo_2O_4$ nanoparticles for high-performance pseudo capacitor, Chemical Engineering Journal, 15766, 2016, DOI: 10.1016/j.cej.2016.09.056.

[72] Hitesh Adhikari, Dipesh Neupane, C.K. Ranaweera, John Candler, Ram K. Gupta, Santosh Sapkota, Xiao Shen, Sanjay R. Mishra, Template-free synthesis of hierarchical mixed-metal cobaltites: Electrocapacitive and Theoretical study, Electrochimica Acta 225 ,514–524, 2016, DOI: 10.1016/j.electacta.2016.12.108.

[73] Subbukalai Vijayakumar, Sadayappan Nagamuthu, Seong-Hun Lee, Kwang-Sun Ryu, Porous thin layered nanosheets assembled $ZnCo_2O_4$ grown on Ni-foam as an efficient electrode material for hybrid supercapacitor applications, International journal of hydrogen energy, Elseiver,48, 2016, DOI: 10.1016/j.ijhydene.2016.09.159.

[74] In Kyu Moon, Seonno Yoon and Jungwoo Oh, 3D Hierarchically Mesoporous $ZnCo_2O_4$ Nanowires Grown on Graphene/Sponge Foam for High Performance Flexible All-Solid- State Supercapacitors, Chemistry - A European Journal, 2016, DOI: 10.1002/chem.201602447.

[75] Yisi Liu, Hao Jiang, Jiayu Hao, Yulong Liu, Haibo Shen, Wenzhang Li, and Jie Li, Metal-Organic Framework Derived Reduced Graphene Oxide Supported $ZnO/ZnCo_2O_4$/C Hollow Nanocages as Cathode Catalysts for Aluminum-O_2 Batteries, ACS Applied Materials & Interfaces, 2017, DOI: 10.1021/acsami.7b08647.

[76] Swati J Patil, Jungsung Park and Dong-Weon Lee, Facial synthesis of nanostructured $ZnCo_2O_4$ on carbon cloth for supercapacitor application, Materials Science and Engineering 282, 012004, 2017, DOI:10.1088/1757-899X/282/1/012004.

[77] A. Juliet Christina Mary and A. Chandra Bose, Facile synthesis of $ZnCo_2O_4$/rGO nanocomposite for effective supercapacitor application, AIP Conference Proceedings 1832, 050093, 2017, DOI: 10.1063/1.4980326.

[78] Saad G. Mohamed, Sayed Y. Attia, Nageh K. Allam, One-step, calcination-free synthesis of zinc cobaltite nanospheres for high-performance supercapacitors, Materials Today Energy 4, 97-104, 2017, DOI: 10.1016/j.mtener.2017.04.003.

[79] Fatin Saiha Omar, Arshid Numan, Navaneethan Duraisamy, Shahid Bashir, K. Ramesh, S. Ramesh, A promising binary nanocomposite of zinc cobaltite intercalated with polyaniline for supercapacitor and hydrazine sensor, Journal of Alloys and Compounds, JALCOM 41769, 2017, DOI: 10.1016/j.jallcom.2017.05.039.

[80] Peng Zhang, Bu Yuan Guan, Le Yu and Xiong Wen (David) Lou, Formation of Double Shelled Zinc-Cobalt Sulfide Dodecahedral Cages from Bimetallic Zeolitic

Imidazolate Frameworks for Hybrid Supercapacitors, Angewandte Chemie International Edition, 2017, DOI: 10.1002/anie.201702649.

[81] A. Juliet Christina Mary, A. Chandra Bose, Surfactant assisted $ZnCo_2O_4$ nanomaterial for supercapacitor application, APSUSC, 2017, DOI: 10.1016/j.apsusc.2018.01.117.

[82] Buddha Deka Boruah, Arnab Maji and Abha Misra, Synergistic Effect in Heterostructure of $ZnCo_2O_4$ and Hydrogenated Zinc Oxide Nanorods for High Capacitive Response, Nanoscale, 2017, DOI: 10.1039/C7NR01644A.

[83] Le Xu, Yan Zhao, Jiabiao Lian, Yuanguo Xu, Jian Bao, Jingxia Qiu, Li Xu, Hui Xu, Mingqing Hua, Huaming Li, Morphology controlled preparation of $ZnCo_2O_4$ nanostructures for asymmetric supercapacitor with ultrahigh energy density, Energy, EGY 10311, 2017, DOI: 10.1016/j.energy.2017.02.018.

[84] Haowen Liu, Qihong Hu, Novel secondary assembled micro/nano porous spheres $ZnCo_2O_4$ with superior electrochemical performances as lithium ions anode material, Nanotechnology - 117002.R2, 2018, DOI: 10.1088/1361-6528/aac456.

[85] Ya Xiong, Zongye Zhu, Degong Ding, Wenbo Lu, Qingzhong Xue, Multi-shelled $ZnCo_2O_4$ yolk-shell spheres for high-performance acetone gas sensor, APSUSC 38647, 2018, DOI: 10.1016/j.apsusc.2018.02.189.

[86] Jai Bhagwan, Goli Nagaraju, Bhimanaboina Ramulu, and Jae Su Yu, Promotive Effect of MWCNT on $ZnCo_2O_4$ Hexagonal Plates and Their Application in Aqueous Asymmetric Supercapacitor, Journal of The Electrochemical Society, 166 (2) A217-A224, 2019, DOI: 10.1149/2.0631902jes.

[87] Yujing Yang, Cui Yang, Kai Tao, Qingxiang Ma, Lei Han, Construction of S-doped $ZnCo_2O_4$ microspindles with enhanced electrochemical performance for supercapacitors, Vacuum 181 109740, 2020, DOI: 10.1016/j.vacuum.2020.109740.

[88] A. Juliet Christina Mary, Clastin Russellraj Indirathankam Sathish, Ajayan Vinu, and Arumugam Chandra Bose, Electrochemical performance of rGO/$NiCo_2O_4$@$ZnCo_2O_4$ ternary composite material and the fabrication of all-solid-state supercapacitor device, American Chemical Society, 2020, DOI: 10.1021/acs.energyfuels.0c01427.

[89] Zixin Dai, Zhiwen Long, Rongrong Li, Chu Shi, Hui Qiao, Keliang Wang, and Ke Liu, Metal−Organic Framework-Structured Porous $ZnCo_2O_4$/C Composite Nanofibers for

High Rate Lithium-Ion Batteries, American Chemical Society, 2020, DOI: 10.1021/acsaem.0c02379.

[90] G. P. Kamble, A. A. Kashale, S. S. Kolekar, I.-W. P. Chen, B. R. Sathe, and A. V. Ghule, Reflux temperature-dependent zinc cobaltite nanostructures for asymmetric supercapacitors, J Mater Sci: Mater Electron, 32:5859–5869, 2021, DOI: 10.1007/s10854-021-05306-w.

[91] Zixin Dai, Zhiwen Long, Chu Shi, Caiqin Wu, Hui Qiao, and Keliang Wang, Porous MOFs–$ZnCo_2O_4$/Carbon Composite Nanofibers for High Lithium Storage, Adv. Electron. Mater., 2100592, 2021, DOI: 10.1002/aelm.202100592.

[92] Noor Hussien AbdAli, Shaymaa Hadi Al- Rubaye, Bahaa H rabee, Kalid Haneen Abass, Electrochemical Performance Enhancement Zinc Cobaltite- Reduced Graphene Oxide for Next Generation Energy Storage Applications, IOP Publishing, 2021, DOI: 10.1088/1742-6596/1818/1/012012.

[93] Ecaterina Magdalena MODAN, Adriana Gabriela, Advantages and Disadvantages of Chemical Methods in the Elaboration of Nanomaterials, 2020, DOI: 10.35219/mms.2020.1.08.

[94] Jiping Zhu, Guangshun Xiao, Xiaolong Li, Synthesis of Li $(Ni_{0.6}Co_{0.2}Mn_{0.2})O_2$ by a modified sol-gel method for lithium-ion batteries, Synthetic Metals 281, 116905, 2021, DOI: 10.1016/j.synthmet.2021.116905.

[95] Andrei A. BunaciuElena Gabriela UdriŞTioiuHassan Y. Aboul-EneinHassan Y. Aboul-Enein, X-Ray Diffraction: Instrumentation and Applications, Critical Reviews in Analytical Chemistry 45(4), 2015, DOI: 10.1080/10408347.2014.949616.

[96] Yogesh Choudhary, J. Lavanya, Gomathi Nageswaran, Electrochemical Characterization, 2017, DOI: 10.1016/B978-0-323-46140-5.00002-9.

[97] NoemieElgrishi, Kelley J. Rountree, Brian D. McCarthy, Eric S. Rountree, Thomas T. Eisenhart, Jillian L. Dempsey; A practical Beginner’s Guide to Cyclic Voltammetry; Journal of Chemical Education, 95, 2018 DOI: 10.1021/acs.jchemed.7b00361.